

Nuclear excitation functions for medical isotope production:
Targeted radionuclide therapy via natIr(d,2n)^{193m}Pt

Hannah Lovise Okstad Ekeberg

June 2020

Contents

| | | |
|----------|--|-----------|
| 1 | Experimental setup | 5 |
| 1.1 | Lawrence Berkeley National Laboratory's 88" Cyclotron | 5 |
| 1.2 | The experiment | 6 |
| 1.2.1 | Target design and foil characterization | 7 |
| 1.2.2 | Irradiation of target stack | 7 |
| 1.2.3 | Counting on high purity detectors | 12 |
| 2 | Analysis | 13 |
| 2.1 | Gamma-ray spectroscopy | 13 |
| 2.1.1 | Energy and peak-shape calibration | 13 |
| 2.2 | Efficiency calibration | 15 |
| 2.3 | End of beam activities | 17 |
| 2.4 | Estimation of the beam current | 17 |
| 2.4.1 | Variance minimization of the deuteron transport calculations | 19 |
| 2.5 | Cross section measurements | 21 |
| 3 | Statistics | 25 |
| 3.0.1 | Radioactive decay law | 26 |
| 4 | Tables | 29 |
| 4.1 | Product nuclei, Q-values and gammarays | 29 |
| 4.2 | Production cross sections | 36 |
| 4.2.1 | $^{nat}Ir(d,x)$ | 36 |

CONTENTS

Chapter 1

Experimental setup

The thin foil stacked-target technique was applied to measure the experimental cross sections for reactions induced in iridium, iron, nickel and copper with deuteron energies ranging from ca. 33-5 MeV. This method is well-described in literature^{1,2} using protons.

1.1 Lawrence Berkeley National Laboratory's 88" Cyclotron

Lawrence Berkeley National Laboratory (LBNL) is a national research laboratory on behalf of the U.S. Department of Energy through its Office of Science, and is operated by University of California, Berkeley. LBNL was founded by Ernest Orlando Lawrence, the inventor of the cyclotron³.

The 88" Cyclotron has many purposes, and can accelerate both light and heavy ions up to Uranium, with a cyclotron number K=140⁴. The cyclotron number is the maximum kinetic energy which can be reached for protons (with no relativistic factors taken into account). The maximum kinetic energy a particle can gain is found from the cyclotron number:

$$\frac{E_k}{A} = K \left(\frac{Q}{A} \right)^2 \quad (1.1)$$

For deuterons with mass number A=2 and charge Q=1, the maximum kinetic energy is $E_k = 70$ MeV. There are multiple programs that takes place in the facility⁵; chip testing and space effects testing, super heavy element searches, fundamental nuclear structure measurements, novel scintillation characterization, fission yield and neutron inelastic scattering measurements (GENESIS) (from Andrew).

A cyclotron is a device that accelerates positively charged particles. It is operated by an alternating electric field, and a perpendicular magnetic field, which by the Lorentz Force forces the particle to accelerate in an outward spiral. The facility is figured in figure 1.1, which consists of a cyclotron vault, and experimental caves in which the beam can be bent to with bending magnets. Faraday cups (not in figure) can measure the beam current at different steps along the tube, which makes it possible to measure the transition efficiency of the beam. Faraday cups are dense metal block, usually 6-7 cm broad Copper and Tantilum. It works as a beam stopper, and can be lowered into the beam line to measure the current. It is electrically isolated, which makes it possible to measure the current, since we know the number of initial particles accelerated. Due to electrons close to surface might be scattered off, it can read off higher positive charge than what is correct. Therefore, a magnet surrounds the cup to bend the electrons back to the Faraday cup in what is called magnetic suppression. Cave 0 is used mainly for neutron beam, chemistry, and isotope production, and was used for irradiation of the target stack.

¹<https://sci-hub.tw/https://doi.org/10.1016/j.nimb.2016.09.018>

²Niobium paper and iron paper from Andrew

³<https://www.lbl.gov/about/>

⁴<http://cyclotron.lbl.gov/home>

⁵<https://ieeexplore.ieee.org/abstract/document/7999622/authorsauthors>

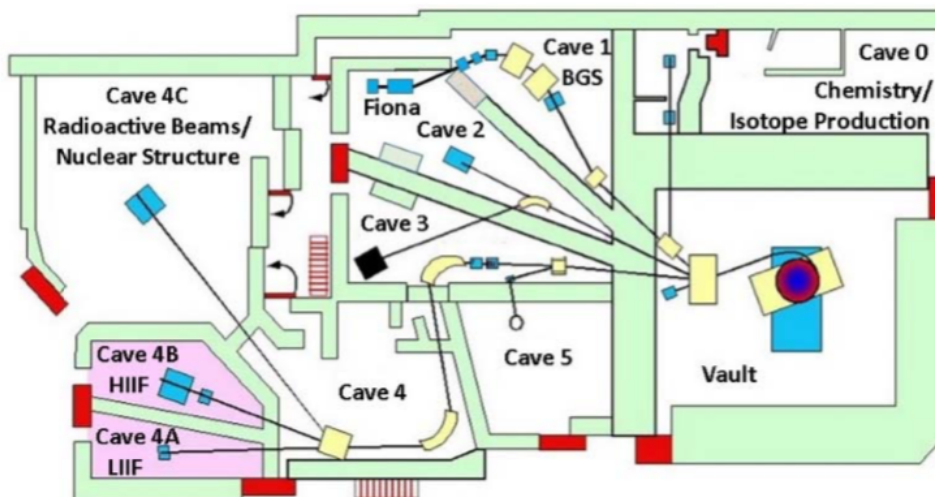


Figure 1.1: An overview of the 88" Cyclotron facility.

<https://cpb-us-e1.wpmucdn.com/sites.usc.edu/dist/7/89/files/2018/04/133-18q03um.pdf>

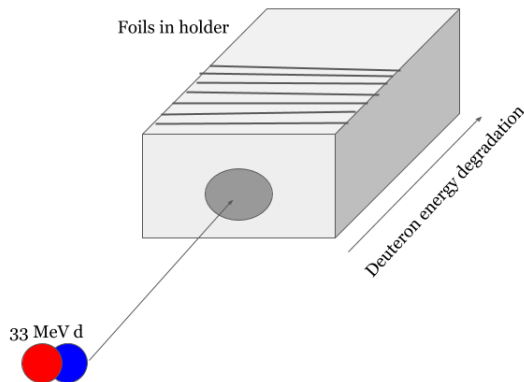


Figure 1.2: The fundamental idea of the experiment where a stack of targets are placed in a target holder, and irradiated with accelerated 33 MeV deuterons. As the energy degrades through the beam stack, it is possible to have multiple cross section measurements at different energies.

1.2 The experiment

The main motivation of this experiment was to measure production cross sections of the products produced after irradiation of a stack of thin iridium foils along with thin monitor foils Nickel, Copper and Iron foils, with a 33 MeV incident deuteron beam, as shown in figure 1.2.

The beam was ca. 1 cm in diameter, and with each target foil being ca. 25 by 25 mm, the beam was underfilled. As the energy was degraded through the stack, multiple cross sections at different energies were possible to measure for the different induced reactions. For production cross section data experiments, thin targets (foils) are used, in the other of a few μm ⁶ are used, since the induced activity is low, meaning that the deadtime of the detector and the dose to human will be low.

Equation ?? is the equation which is used in the calculation of the cross sections. In order to calculate the cross section of a product, end of beam activity, number of target nuclei and beam current must be found, where for the end of beam activity, the detector efficiency need to be estimated. The number of target nuclei was estimated through characterization of the foils. A_0 was estimated using equation

⁶(Syed M. Qaim. Nuclear data for production and medical application of radionuclides: Present status and future needs. Nuclear Medicine and Biology, 44:31–49, jan 2017.)

3.28, which depends on the efficiency calibration of the detectors as a function of gamma-ray energy, the number of counts registered and the intensity of the gamma-rays emitted by the source, the decay constant of the source and the delay time. Some of the nickel, copper and iron deuteron-induced cross section are well-established, and can be used to determine the beam current throughout the stack.

1.2.1 Target design and foil characterization

In this experiment, the target stack was composed of ten natural iridium foils (99.9%) foils, along with ten natural nickel foils (..%), ten natural copper foils (..%) and three natural iron foils (..%) (from Goodfellow Corporation, Corapolis, PA 15108, USA) serving as monitor foils. Along with two stainless steel foils in the front and the back of the stack, a proton degrader (a 6061 aluminum alloy), and an extra nickel neutron monitor foil was used to obtain production cross sections at multiple energies, using one incident deuteron beam. The full order of the stack and the characterization of each foil can be seen in table 1.1.

Each foil were cut into approximately 25 by 25 mm squares, and each foil was characterized using a caliper (Mitutoyo Absolute Digimatic) to measure the length across each side, a gauge caliper (Mitutoyo IP65 Coolant Proof) to measure the thickness and an analytical balance weight (Mettler Toledo) to measure the mass of each foil which was prewashed with isopropanol. For each measurement, the unit was measured 4 times, and the values listed in table 1.1 are averaged values. The length and mass were used to measure the mass density. The thickness was not used in the calculation of the mass density, but was a good indication that the foil thicknesses were consistent. **For underfilled beams, the mass density of the foil is used to find the number of nuclei per cm², by using the area of each foil.** The mass density was calculated using the mass of each foil divided by the area

$$\rho\Delta r = \frac{m}{A} \quad (1.2)$$

The uncertainty in each parameter was calculated using the standard deviation (equation 3.2) of the four measurements per unit, and the total uncertainty was calculated using the approximation of uncorrelated variables used in equation 3.13. The conversion from mg per cm² to nuclei per cm² was done numerically, by multiplying the mass density with Avogadro's number N_A and dividing by the mol-mass of the target atoms.

After the characterization, each foil was mounted on a plastic frame with an open space in the middle and attached with capton tape along the edges (from previous experiments, capton tape have shown to be a large **proton?** degrader, so it was important that the tape was not in the beamline **Article by Andrew**). The target frames can be seen in figure 1.3.

1.2.2 Irradiation of target stack

The irradiation included tuning of the beam and one hour of radiation over the target stack. Whenever the beam was turned on, the beam tube had to be pumped down to a vacuum, to not attenuate the beam. The target holder was a 6061 aluminum alloy with a hole in the front for the beam. The targetholder was placed in the end of the beam tube (**mounts of the end of an electrically-isolated beamline, (iron paper andrew)**). The targetholder can be visualized in figure 1.4, with a spring holding the foils stable (??a) and placed in the end of the beam tube (??b).

Tuning the beam

The cyclotron was tuned for a 33 MeV deuteron beam, and needed to have the correct beam spot. First, the beam spot was visualized using a ca. 2.5 cm thick borosilicate glass, painted with a mixture of phosphor powder and vacuum grease (so that the paint does not evaporate as the tube was pumped down to vacuum). When ionizing radiation strikes the phosphor, the phosphor is excited and emits light in the de-excitation, called phosphorescence. The glass is placed on the end of the beam tube. With a camera placed in cave 0, from the control room, the beam spot could be visualized, and could

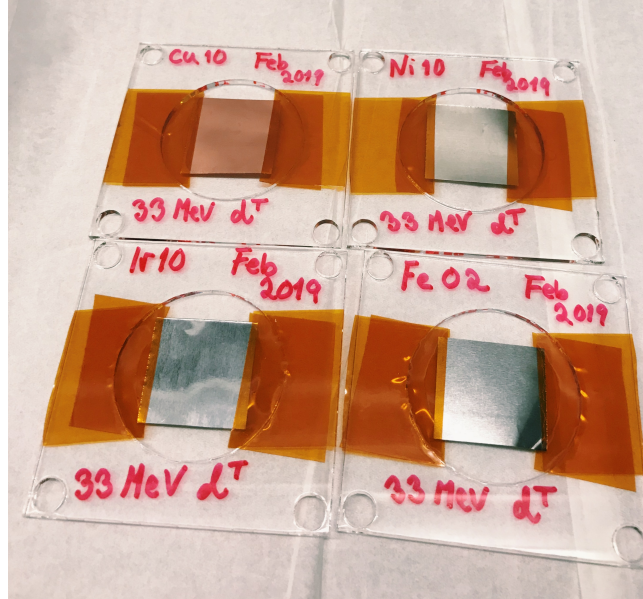


Figure 1.3: The figure shows the four different targets mounted on plastic frames with capton tape attached along the edges of the foils.

be steered to be centered and ca. 1 cm in diameter. Secondly, visualization of the beam throughout the beam stack was important to see that the beam did not diverge converge/diverge or move in the wrong direction over the target stack. Gafchromic films which change color if struck by ionizing radiation was placed in the front and the back of the target holder, separated by the spring. The films were exposed for a brief second, and the blue spot was evaluated. This was done until the beamspot was good both in the front and in the back of the stack.

The beam efficiency transmission was calculated by measuring the current at the Faraday cup right after the cyclotron vault (BS-02) and right before cave 0 (FC-01). BS-02 was measured to be 420 nA and FC-01 was measured to be 285 nA. This gave beam efficiency of transmission

$$\frac{FC - 01}{BS - 02} = 67\%$$

Irradiation of the target stack

The targetstack was irradiated for exactly an hour, and the current was read of the beam integrator evenly, to assure that the it increased constantly. The beamcurrent from the beam integrator read 128.5 nA. Right after end of beam, the targets were sealed in plastic bags to avoid contamination. The foils were counted at the seven different detectors for the following 4 weeks after end of beam, first short counts to get as many observations as possible of the short-lived activities and longer and longer counts as the times since end of beam passes, so that the counting statistics for the longer lived activites are good.

Intensity profile of the beam

After irradiation, gafchromic film were attached to the activated stainless steel in the front and the back of the stack, to obtain an intensity profile of the beam. The radius of the activity from stainless on gafchromic film is used in the imaging process program Image-J, which can be seen on figure 1.5. The gafchromic films were scanned, and the intensity data (**x and y arrays**) were obtained by inverting the scanned image, and drawing a line segment along the beam spot that automatically created an position dependent intensity array. The intensity profile can be fitted to a Gaussian, which is shown examplewise in figure 1.6, which is the horizontal beam profile in the front and the back of the stack. In the assumption that the beam was underfilled, it was important to build confidence in that the

Table 1.1: Characterization of each foil, along with calculated mass density. Each length is measured in mm, and mass in grams.

| Foil | Length1 (mm) | Length2 (mm) | Thickness (mm) | Mass (g) | Mass density (mg/cm ²) |
|--------------------|--------------|--------------|----------------|----------|------------------------------------|
| SS1 | ... | | | | |
| Ni01 | 25.228 | 25.293 | 0.0285 | 0.1453 | 22.772 ± 0.138 |
| Ir01 | 24.943 | 24.968 | 0.0295 | 0.3436 | 55.174 ± 0.053 |
| Cu01 | 25.553 | 24.883 | 0.0341 | 0.1420 | 22.338 ± 0.048 |
| Fe01 | 24.400 | 26.068 | 0.0278 | 0.1274 | 20.030 ± 0.110 |
| Ni02 | 25.288 | 25.428 | 0.0295 | 0.1487 | 23.118 ± 0.096 |
| Ir02 | 24.923 | 25.005 | 0.0278 | 0.3465 | 55.601 ± 0.238 |
| Cu02 | 25.443 | 25.550 | 0.0348 | 0.1451 | 22.325 ± 0.028 |
| Fe02 | 25.525 | 23.800 | 0.0274 | 0.1216 | 20.017 ± 0.034 |
| Ni03 | 25.295 | 25.210 | 0.0270 | 0.1425 | 22.338 ± 0.066 |
| Ir03 | 24.885 | 24.983 | 0.0243 | 0.3459 | 55.643 ± 0.121 |
| Cu03 | 25.560 | 25.508 | 0.0343 | 0.1455 | 22.313 ± 0.043 |
| Fe03 | 26.113 | 25.235 | 0.0310 | 0.1315 | 19.948 ± 0.114 |
| Ni04 | 25.303 | 24.888 | 0.0273 | 0.1304 | 20.704 ± 0.068 |
| Ir04 | 24.960 | 24.833 | 0.0261 | 0.3471 | 56.000 ± 0.109 |
| Cu04 | 25.153 | 25.603 | 0.0333 | 0.1435 | 22.284 ± 0.027 |
| Ni05 | 25.325 | 25.495 | 0.0263 | 0.1406 | 21.768 ± 0.045 |
| Ir05 | 24.948 | 24.958 | 0.0256 | 0.3435 | 55.161 ± 0.081 |
| Cu05 | 25.213 | 25.573 | 0.0334 | 0.1447 | 22.443 ± 0.028 |
| Ni06 | 25.530 | 25.195 | 0.0285 | 0.1471 | 22.861 ± 0.123 |
| Ir06 | 24.760 | 24.960 | 0.0240 | 0.3444 | 55.731 ± 0.088 |
| Cu06 | 25.343 | 25.513 | 0.0340 | 0.1448 | 22.396 ± 0.012 |
| Ni07 | 25.338 | 25.278 | 0.0268 | 0.1479 | 23.092 ± 0.078 |
| Ir07 | 24.955 | 25.008 | 0.0278 | 0.3538 | 56.685 ± 0.085 |
| Cu07 | 25.625 | 25.248 | 0.0326 | 0.1444 | 22.320 ± 0.014 |
| Ni08 | 25.205 | 24.950 | 0.0256 | 0.1409 | 22.409 ± 0.124 |
| Ir08 | 24.723 | 24.985 | 0.0281 | 0.3585 | 58.030 ± 0.130 |
| Cu08 | 25.370 | 24.885 | 0.0333 | 0.1414 | 22.401 ± 0.033 |
| Ni09 | 25.220 | 25.378 | 0.0257 | 0.1392 | 21.741 ± 0.073 |
| Ir09 | 24.670 | 24.993 | 0.0273 | 0.3494 | 56.669 ± 0.043 |
| Cu09 | 25.390 | 26.455 | 0.0331 | 0.1506 | 22.425 ± 0.041 |
| Ni10 | 25.285 | 24.405 | 0.0271 | 0.1425 | 23.093 ± 0.024 |
| Ir10 | 24.973 | 24.980 | 0.0270 | 0.3435 | 55.065 ± 0.055 |
| Cu10 | 25.470 | 25.338 | 0.0355 | 0.1440 | 22.314 ± 0.047 |
| SS2 | ... | | | | |
| P-degrader | ... | | | | |
| Ni neutron monitor | ... | | | | |

beamspot was ca. 1 cm in diameter, which was done estimating the full width half maximum of the Gaussian profile. The FWHM over SS1 was 1.2017 cm horizontally ($\sigma^2 = 0.2604 \text{ cm}^2$) and 1.1420 cm vertically ($\sigma^2 = 0.2352 \text{ cm}^2$). The FWHM over SS2 was 0.6706 cm horizontally ($\sigma^2 = 0.0811 \text{ cm}^2$) and 0.5783 cm vertically ($\sigma^2 = 0.0603 \text{ cm}^2$).

Normally the beam broadens throughout the stack due to scattering. As we can see, this is not the case, since the beam is stopped in the targetstack, and therefore we do not know how much the beam truly scatters. This gives a higher uncertainty. The stainless steel (which consists of ..) has fast decay time. However since it emits beta-particles, the radius will slightly increase, and the true beam spot is slightly smaller. Thus the estimated FWHM values for SS1 seem to be within the criterion for underfilled targets.



(a) The target stack in target holder

(b) Target holder placed in the end of beam tube

Figure 1.4: Figure shows the target stack and how it was placed in the beam tube.

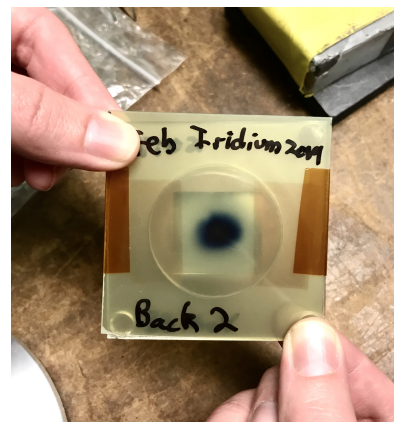
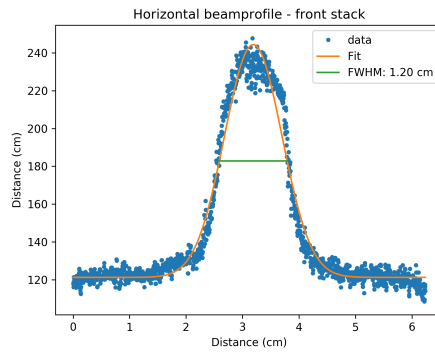
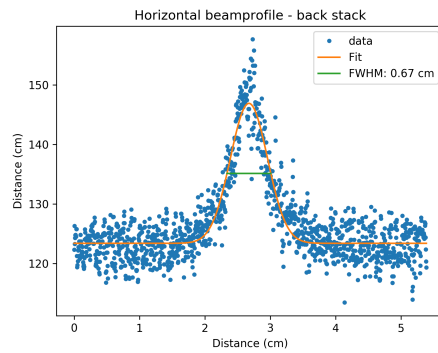


Figure 1.5: The gafchromic film on the activated SS1 foil.



(a) Horizontal intensity profile of SS1



(b) Horizontal intensity profile at SS2

Figure 1.6: Figure shows the intensity profile of the deuteron beam in the front and in the back of the stack horizontally.



Figure 1.7: The calibration point sources that were used in the efficiency calibration of the detector. (^{22}Na was excluded because it was difficult to work with.)

Table 1.2: The calibration point sources along with gamma lines used in the calibration of the detectors. * indicates that the value has been averaged over two peaks with similar energy, less than 1 keV. For the intensity its just added together.

| ^{137}Cs | | ^{133}Ba | | ^{152}Eu | |
|------------|------------|------------|------------|------------|------------|
| E_γ | I_γ | E_γ | I_γ | E_γ | I_γ |
| 32.005* | 5.63* | 53.1622 | 2.14 | 121.7817 | 28.53 |
| 36.3405* | 1.02* | 80.9979 | 32.9 | 244.6979 | 7.55 |
| 661.657 | 85.10 | 160.6120 | 0.638 | 295.9387 | 0.440 |
| | | 223.2368 | 0.453 | 344.2785 | 26.5 |
| | | 276.3989 | 7.16 | 367.7891 | 0.859 |
| | | 302.8508 | 18.34 | 411.1165 | 2.237 |
| | | 356.0129 | 62.05 | 244.4853* | 3.125* |
| | | 383.8485 | 8.94 | 503.467 | 0.1524 |
| | | | | 586.2648 | 0.455 |
| | | | | 678.623 | 0.473 |
| | | | | 688.670 | 0.856 |
| | | | | 719.353* | 0.345* |
| | | | | 778.9045 | 12.93 |
| | | | | 810.451 | 0.317 |
| | | | | 867.380 | 4.23 |
| | | | | 963.712* | 14.65* |
| | | | | 1112.076 | 13.67 |
| | | | | 1212.948 | 1.415 |
| | | | | 1299.142 | 1.633 |
| | | | | 1408.013 | 20.87 |

1.2.3 Counting on high purity detectors

Seven different detectors were used, six IDM Ortec detectors (detectors 1-6) with detector diameter 85 mm, detector length 30 mm and hole depth 15 mm, and one Germanium detector (detector 7) with detector diameter 64.9 mm, detector length 57.8 mm and hole depth 48.6 mm **from detector diagrams**. Besides, IDM detectors were located in cave 4c (see figure 1.1), which have previously been used as radiation chamber. Thus, background radiation was present. For detector 7, there was led shielding around the detector. Spectra taken on the Germanium detector is preferred. In order to visualize the signal from the detector, Maestro (Multichannel Analyzer Emulation Software⁷) was used.

The detectors were calibrated for efficiency, peak shape and gamma-ray energy using ^{137}Cs ($t_{1/2} = 30.08$ years[?]), ^{133}Ba ($t_{1/2} = 10.551$ years[?]) and ^{152}Eu ($t_{1/2} = 13.517$ years[?]) point sources, using the gammalines listed in table 1.2. The calibration was done at various distances from the detector surface. The point sources can be seen on figure 1.7. The energy and peakshape calibration was done in FitzPeakz which is described in section 2.1.1. The efficiency calibration is described in section 2.2.

The iridium foils were counted within 15 minutes after end of beam, and the other foils following up after. All the foils were counted for ca. four weeks following end of beam, with short counts in the beginning to have good statistical data for the short-lived activities, and longer and longer counts as the shorter and medium-lived activities decayed out, to have good statistics (enough counts). Since the detectors were calibrated at various distances, the deadtime of the foils right after end of beam could be reduced, however, as high as 16-22% deadtime was present, but reduced to less than 5% within a certain time after end of beam.

⁷<https://www.ortec-online.com/products/application-software/maestro-mca>

Chapter 2

Analysis

The analysis of estimating production cross sections consisted of multiple steps. To obtain the end of beam activities the peak areas (number of counts) were found with gamma-ray spectroscopy using FitzPeakz¹. The efficiency calibration as a function of gammaray energy was done using ¹³⁷Cs, ¹³³Ba and ¹⁵²Eu point sources. The energy degradation in the foils were simulated using NPAT², giving the deuteron flux as a function of energy. Along with the simulation and IAEA recommended cross sections for the monitor reactions³, the weighted average beam current was estimated in each foil.

2.1 Gamma-ray spectroscopy

The spectra were analyzed in FitzPeakz⁴. The mathematic algorithm in which FitzPeakz is based upon is SAMPO80⁵. The peaks are assumed Gaussian with an exponential tail on both sides of the peak. The exponential tail and Gaussian function are joined so function and first derivative are continuous. The algorithm searches for peaks by using the smooth second difference (derivative?) Particularly good for detecting small peaks on a high or low background. The peak areas are calculated by fitting the precalibrated modified Gaussian to the data with a weighted least squares formula using a parabolic background. Fitting intervals are determined automatically by the program. Peaks separated by less than 4 times the average fwhm are fitted together.

For each spectra, a report file containing peak energy, centre channel, full width half maximum, significance, goodness of fit, peak area, uncertainty in peak area, gammas per second, uncertainty in gammas per second and a background estimation for each peak was provided. The most important parameters were the energy, the peak area N_C and uncertainty in peak area. Peak area was needed for the activity calculation in equation 3.28 which is an important parameter in the calculation of the cross section (equation ??), and in the calculation of the efficiency for the calibration sources (equation 2.1). Gammas per second (also called countrate) was used to get an indication if the rate of gammas, which were used as a critical tool to evaluate background contamination in a peak for instance.

Figure 2.1 shows an example of a gamma ray spectrum for one of the iridium spectra (Ir05) approximately 35 hours after end of beam. Figure 2.2 shows the X-ray region and gamma region of ^{193m}Pt.

2.1.1 Energy and peak-shape calibration

Used calibration sources ¹³⁷Cs ($t_{1/2} = 30.08$ years[?]), ¹³³Ba ($t_{1/2} = 10.551$ years[?]) and ¹⁵²Eu ($t_{1/2} = 13.517$ years[?]), which can be seen on figure 1.7.

The calculated peak locations and areas are finally corrected with energy and efficiency calibration data to yield peak energies and intensities. For the energy calibration, linear interpolation on a linear

¹<https://www.jimfitz.co.uk/fitzpeak.htm>

²<https://pypi.org/project/npat/>

³https://www-nds.iaea.org/medical/monitor_reactions.html

⁴<https://www.jimfitz.co.uk/fitzpeak.htm>

⁵[https://sci-hub.tw/https://doi.org/10.1016/0029-554X\(81\)90209-3](https://sci-hub.tw/https://doi.org/10.1016/0029-554X(81)90209-3)

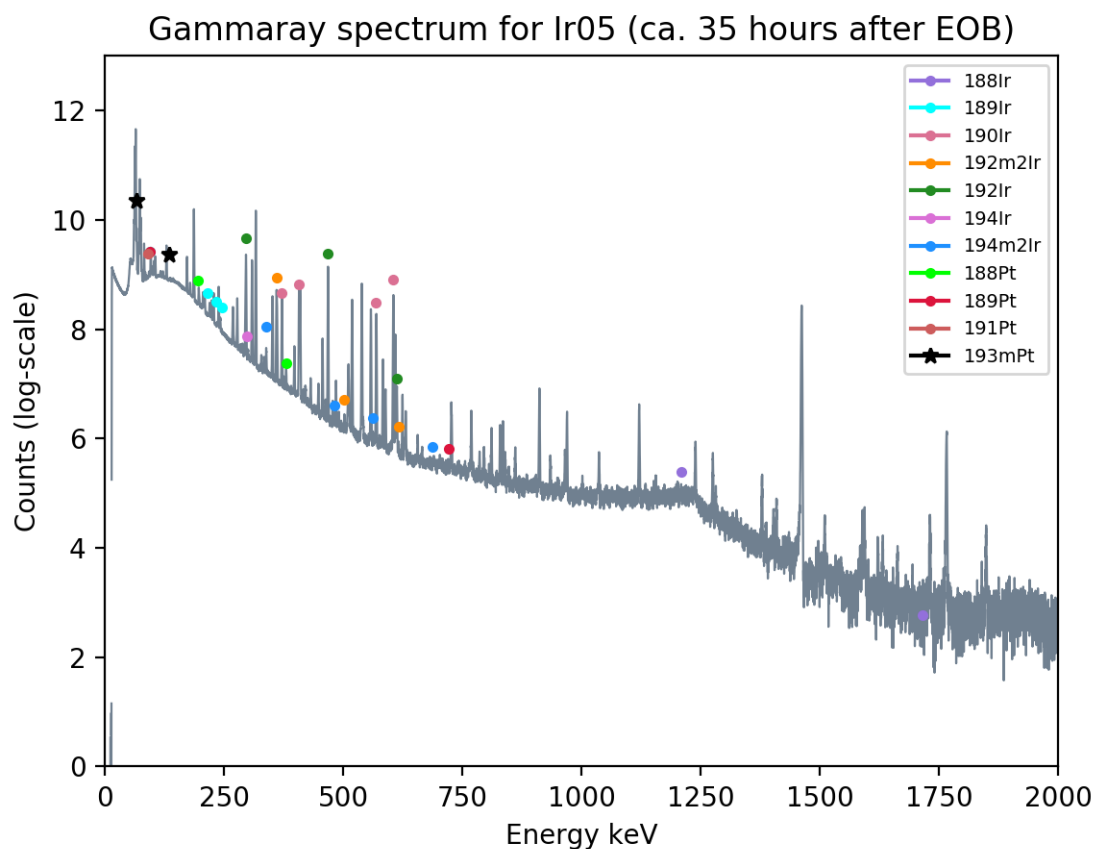


Figure 2.1: Gammaray spectrum for Ir05 taken approximately 35 hours after end of beam. Nuclei does not necessarily represent what is present in the spectrum, but where the peak would have been. Hard to include all since there are different decay times.

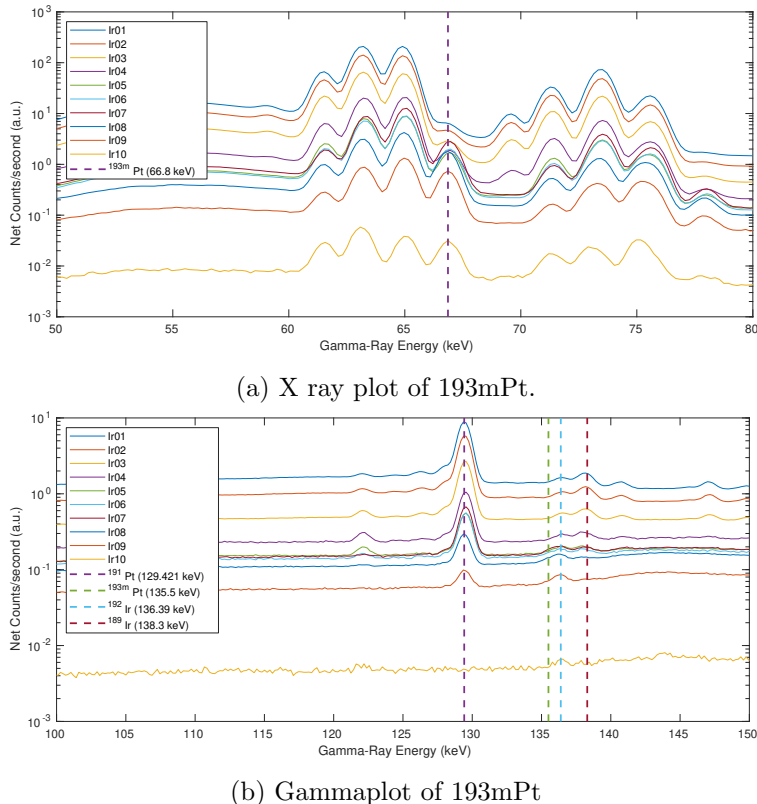


Figure 2.2: Which spectra are these??

scale and for the efficiency calibration linear interpolation on a log-log scale are used in this code. Calibration errors are added to the peak location and intensity errors to give the final result (p.94). The peak shape calibration uses 7 parameters; two background peaks, peak height and location, peak width, distance from peak centroid to the starting point of exponential on either side. The minimization of the least-squares expression to solve for the peak parameters is done by a subroutine package with an iterative gradient algorithm utilizing the variable metric method. Minimization is terminated when all components in the next step change by less than 10^{-8} , if four succeeding values of χ^2 are the same or if 100 iterations have been completed. The performed shape calibration can be checked with a few parameters, goodness of fit, χ^2 per degree of freedom, sigma and error correlation. Sigma below 5 and error correlation between -1 and 1 are acceptable values. (p.90)

From the webpage [jim-fitzy.com/calib.html](http://www.jim-fitzy.com/calib.html): Each detector was calibrated with peak shape and energy for the calibration sources. Fitzpeakz takes in energy (.enc) and peak shape (.shp) calibration source files, containing the energies listed in table 1.2. For the peak shape, the program determines the parameters of width and the amount of low energy tailing. The energy calibration and peak shape calibration was estimated to a 1st order function.

2.2 Efficiency calibration

The efficiency calibration is an important factor in the calculation of the cross section in equation ???. The detector efficiency is the number of events registered divided by the events emitted by the source. The absolute efficiency can be divided into intrinsic and geometrical efficiency, where the intrinsic efficiency is the number of events registered divided by the number of events hitting the detector. The intrinsic efficiency thus depends on the interaction cross section between incident particle and detector material. For neutral particles, the size of the detector affects the intrinsic efficiency, the larger crystal the larger the probability of interaction is. The geometrical efficiency is the radiation emitted by the source which hits the detector. (Techniques for Nuclear and Particle Physics Exper-

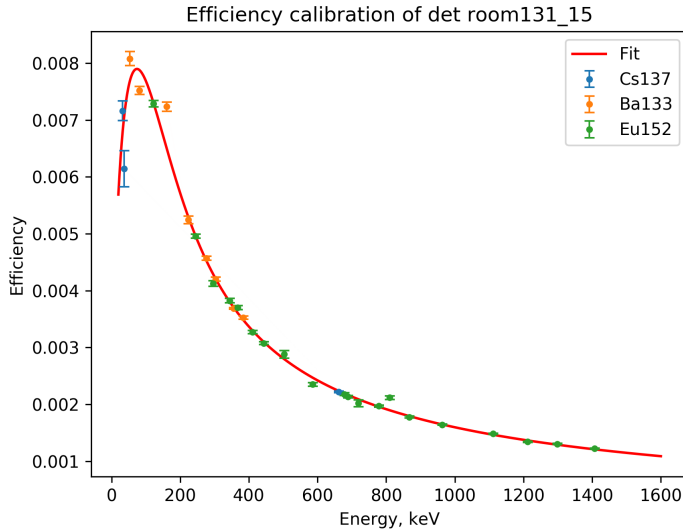


Figure 2.3: An example of an efficiency curve with exact points calculated from equation 2.1 and a curve fit from equation 2.2.

iments. William R. Leo. Second Revised Edition. Springer.Verlag Berkling Heidelberg GmbH, New York (1994). p. 121-122)

The efficiency was measured using calibration point sources ^{137}Cs ($t_{1/2} = 30.08$ years[?]), ^{133}Ba ($t_{1/2} = 10.551$ years[?]) and ^{152}Eu ($t_{1/2} = 13.517$ years[?]). Figure 1.7 shows the calibration points sources (^{22}Na was excluded during the data-analysis since it only contains a single gamma-line and gave poorer results). On each calibration source, a reference date is given with an activity, which here is referenced to as A_0 of the calibration sources.

Solving Equation 3.28 for efficiency, ϵ , the analytical efficiency as a function of gamma-ray energy and intensity is

$$\epsilon(E_\gamma) = \frac{N_C \lambda}{A_0 I_\gamma (1 - e^{-\lambda \Delta t_c}) e^{-\lambda \Delta t_d}} \quad (2.1)$$

where λ is the decay constant and N_C is the number of counts in the measured spectra, and Δt_d is the delay time since the reference date. The analytical efficiency gives one single value for the efficiency at energy E_γ , but we want a continuous function which gives the efficiency at any gamma-energy. A model based upon Gallagher, W. J., Cipolla, S.J. (1974) was applied which takes the probability of penetration through the deadlayer of the detector and the probability of interaction in the detector volume into account

$$\epsilon(E_\gamma) = B_0 + \underbrace{(e^{-B_1 E_\gamma^{B_2}})}_{\text{dead layer}} \underbrace{(1 - e^{-B_3 E_\gamma^{B_4}})}_{\text{interacting with volume}} \quad (2.2)$$

where B_i is optimum parameters minimizing the χ^2 in the scipy optimizing curve fit function⁶). Figure 2.3 shows an example of an efficiency curve for a detector at a specific distance from the detector. The uncertainty of the efficiency was estimated using equation 3.6 numerically. For each source, the gamma-lines with the intensities which were used to calculate the efficiency points for each source is listed in table 1.2.

⁶https://docs.scipy.org/doc/scipy/reference/generated/scipy.optimize.curve_fit.html

2.3 End of beam activities

The end of beam activities were estimated by extrapolating backwards in time, with the measured activities at various timepoints after the end of beam. The activities as a function of time since EOB was calculated using equation 3.27, along with a self-attenuation correction:

$$A(\Delta t_d) = \frac{N_C \lambda}{\epsilon_\gamma (1 - e^{-\lambda \Delta t_d}) e^{-\mu \rho \Delta r / 2}} \quad (2.3)$$

where μ is the photo attenuation coefficients from the XCOM photon cross section database⁷, and $\rho \Delta r$ is the mass density of the foil. The gammas which were used are listed in tables 4.2, 4.1, 4.3 and 4.4 for iron, nickel, copper and iridium respectively. The gamma-ray self-attenuation (which is typically less than 0.2 % (Iron paper, Andrew)) correction is based on the assumption that all activity that is made is located midway in the foil thicknesses. In reality however, the activity profile will follow the same shape as the excitation function over the energy range that expands over the foil, if we assume that the stopping power $dE/dx=0$ which is a good estimation for thin foils less than 100 mg/cm²?? (since activity and cross section are proportional). We do not know the excitation function ahead of time, and the excitation function does not change much either, since the foil thicknesses are so thin. So instead, this simplification is done, assuming that the average attenuation is through half of the foil thickness.

The equation describing the shape of the decay curve is given in equation 3.16 for single decay or 3.17 for multiple decay. Decay chains of single and two-step decay ($n=1,2$) was sufficient in this analysis;

$$A = A_0 e^{-\lambda \Delta t_d}, \quad \text{single step decay} \quad (2.4)$$

and

$$A_2(t) = \lambda_n \left[A_{1,0} \lambda_1 \frac{(e^{-\lambda_1} + e^{-\lambda_2})}{\lambda_1 - \lambda_2} + A_{2,0} e^{-\lambda_2 t} \right], \quad \text{two step decay} \quad (2.5)$$

where subnumber 1 is the parent nucleus, and subnumber 2 is the daughter nucleus. Parent activity is calculated from single step decay. The uncertainty was treated as covarianced variables?

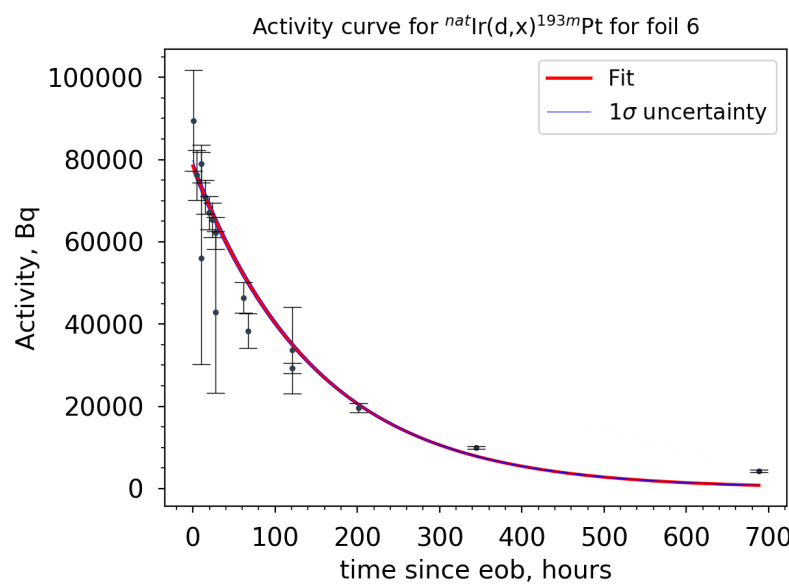
The way in which the extrapolation was done was the scipy optimize curve fit function, where the A_0 of the daughter was the optimizing parameter. Since there is only one optimized parameter, there was no covariance and the uncertainty was calculated using equation 3.13. In the cases where neither parent or daughter activity were known, which were the case for the monitor reaction ⁵⁸Co with ^{58m}Co decaying into the ground state by internal conversion, both parent and daughter activity were optimizing parameters which are very correlated and thus the uncertainty in end of beam activity was calculated 3.6. Figure 2.4 shows two examples of the two different activity curves; one step decay for ^{193m}Pt ($t_{1/2}=4.33$ days) and two step decay for the monitor product ⁵⁸Co ($t_{1/2}=70.86$ days) with feeding from the isomer ^{58m}Co ($t_{1/2}=9.10$ hours).

2.4 Estimation of the beam current

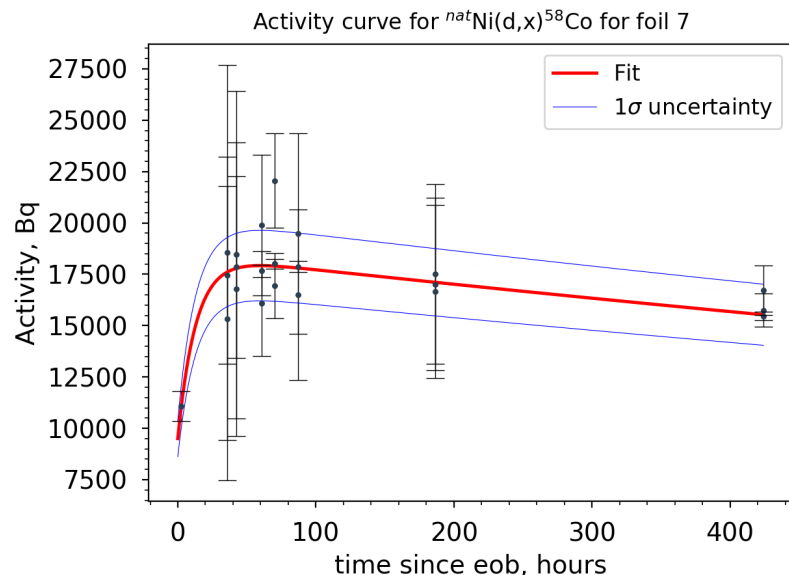
The beamintegrator measured a current of 128.5 nA in front of the beam stack. However in order to have precise cross section measurements, the beamcurrent in each foil was estimated. The IAEA recommended monitor reactions (2017) ^{nat}Ni(d,x)⁶¹Cu, ^{56,58}Co, ^{nat}Cu(d,x)^{62,63,65}Zn and ^{nat}Fe(d,x)⁵⁶Co were used to obtain a weighted average beam current in each foil solving equation 3.28 for beam current Φ :

$$\Phi(E) = \frac{A_0}{N_T \sigma(E)_{\text{mon}} (1 - e^{-\lambda \Delta t_{\text{irr}}})} \quad (2.6)$$

⁷<https://www.nist.gov/pml/xcom-photon-cross-sections-database>



(a) Activity of ^{193m}Pt ($t_{1/2}=4.33$ d) produced from iridium. The end of beam activity was estimated using a one step decay (equation 2.4)



(b) Activity of ^{58}Co ($t_{1/2}=70.86$ d) produced from nickel. The end of beam activity is estimated using a two step decay (equation 2.5. The feeding is from ^{58m}Co ($t_{1/2}=9.10$ h.)

Figure 2.4: Two examples of activity curves. The uncertainty in activity decreases with increasing time since end of beam which is due to longer counts decreases the uncertainty. (from theory, counting statistics)

Equation 2.6 builds upon the thin target assumption, which implies that the energy degradation $dE/dx=0$. However, we know that there is an energy distribution, which was estimated using NPAT's (Nuclear Physics Analysis Tool) Ziegler simulation. The ziegler code simulates the deuteron transport based upon the Anderson & Ziegler stoppingpower formalism, using Monte Carlo simulations **write a few sentences in theory...** The code provides the full deuteron energy and flux degradation in each foil, $d\phi/dE$, which can be visualized for the iridium foils in figure 2.5. Can be seen that as the deuteron energy is degraded, the mean value is shifted towards the low energy side, and the peak width increases. As stoppingpower is inversely proportional to the charge particle energy ($-\frac{dE}{dx} \propto \frac{1}{\beta^2}$, bethe block), and along with scattering taking place towards the end of stack, the low energy tail is more degraded, and we see a skew towards the low energy, creating a broader energy-flux profile and a shift of the mean value (centroid). This shift leads to an increasing uncertainty in energy. The (normalized) flux-weighted average energy for each foil was calculated, **ironpaper: which takes into account the slowing down of deuterons, and reports effective energy centroid of each foil**, using the energy distributions $d\phi/dE$ provided by the Ziegler code:

$$\langle E \rangle = \frac{\int E \frac{d\phi}{dE} dE}{\int \frac{d\phi}{dE} dE} \quad (2.7)$$

The uncertainty in beam energy is divided into low energy and high energy tale, with the FWHM split by the centroid (figure 2.5).

Likewise, the energydependent monitor IAEA cross sections need to be flux-weighted over each foil. In order to do this, a spline interpolation over the energy array over each foil provided by the Ziegler simulation was spline interpolated with the IAEA recommended cross section data. Thus, the monitor cross section in equation 2.6 is modified to

$$\sigma(\langle E \rangle) = \frac{\int \sigma_{\text{mon}} \frac{d\phi}{dE} dE}{\int \frac{d\phi}{dE} dE} \quad (2.8)$$

With the end of beam activities for the monitor reactions, number of target nuclei and the flux-weighted IAEA cross sections, the beam current as a function of the flux-weighted average beam energy was estimated for each reaction in each foil.

2.4.1 Variance minimization of the deuteron transport calculations

In theory, the estimated beam current of a charge particle beam should be constant, until completely stopped, since the majority of the incident particles does not interact in nuclear reactions, but only lose energy via elastic and inelastic scattering. However, non-consistant values of the beam current, especially in the back of the stack can be due to energy bins being assigned wrongly in the energy distribution simulation done in Ziegler or a systematic error in the areal density which gets progressively worse further back in the stack (Niobium paper, Andrew). A way to work around these errors was to perform a variance minimization varying the beam energy and the areal density of the foils with 20% increase and decrease systematically, and estimate the reduced χ^2 (equation 3.4) over compartment 3,6 and 9. Variance minimization (Andrew's Niobium and iron paper + <https://sci-hub.tw/https://doi.org/10.1016/j.nimb.2016.09.018>).

For compartment 3 ($E_d=25$ MeV) all seven monitor reactions were above threshold, thus 6 degrees of freedom. However, early in the target stack, the scattering was low, and the χ^2 does not tell how well the energy bin assignment work further back in the stack. For compartment 6 ($E_d=18$ MeV), all the six possible monitor reactions (for nickel and copper) were above threshold, and it gave a good estimate of how the beam current was developing throughout the stack. In compartment 9 ($E_d=10$ MeV), five monitor reactions are above threshold (except for ^{62}Zn). At the very end it is possible to see the full effect of the scattering.

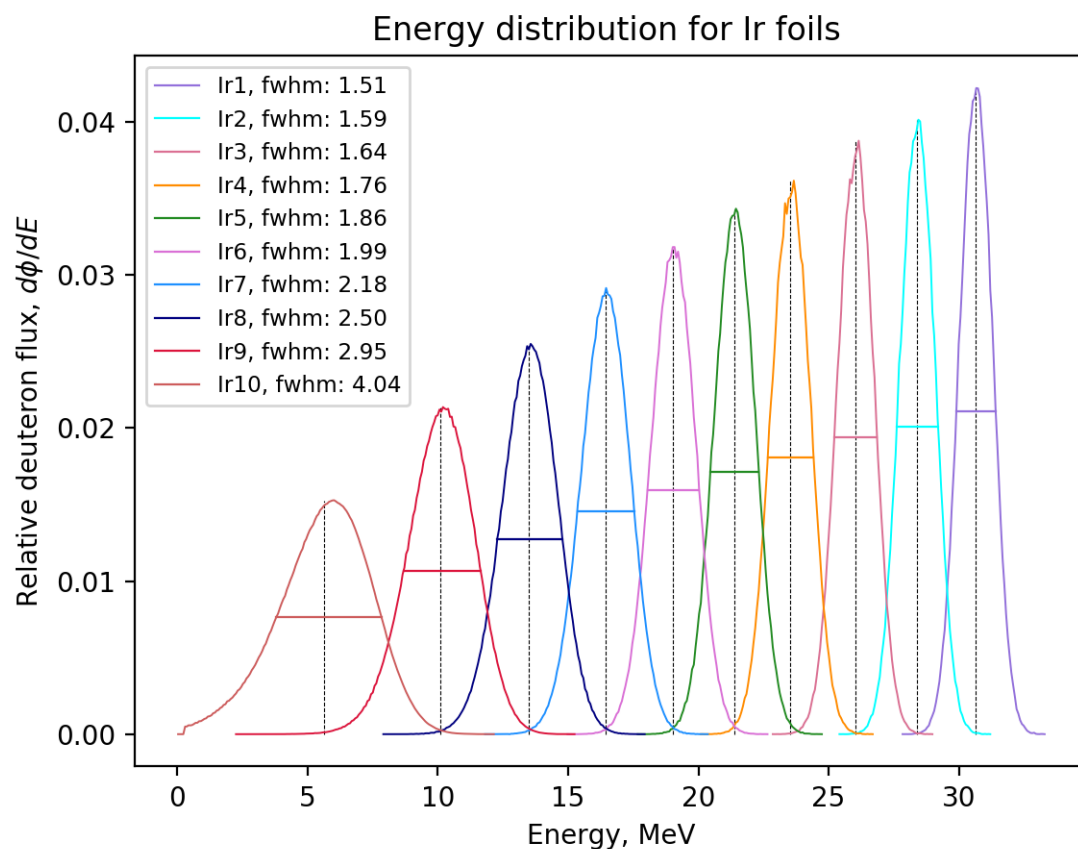


Figure 2.5: Iridium energy flux distribution over the 10 foils. As the energy degrades, skewed and larger full width half max. The vertical line in each peak is the mean value. This indicates that at lower energies, the right uncertainty is greater than the left uncertainty in the peak.

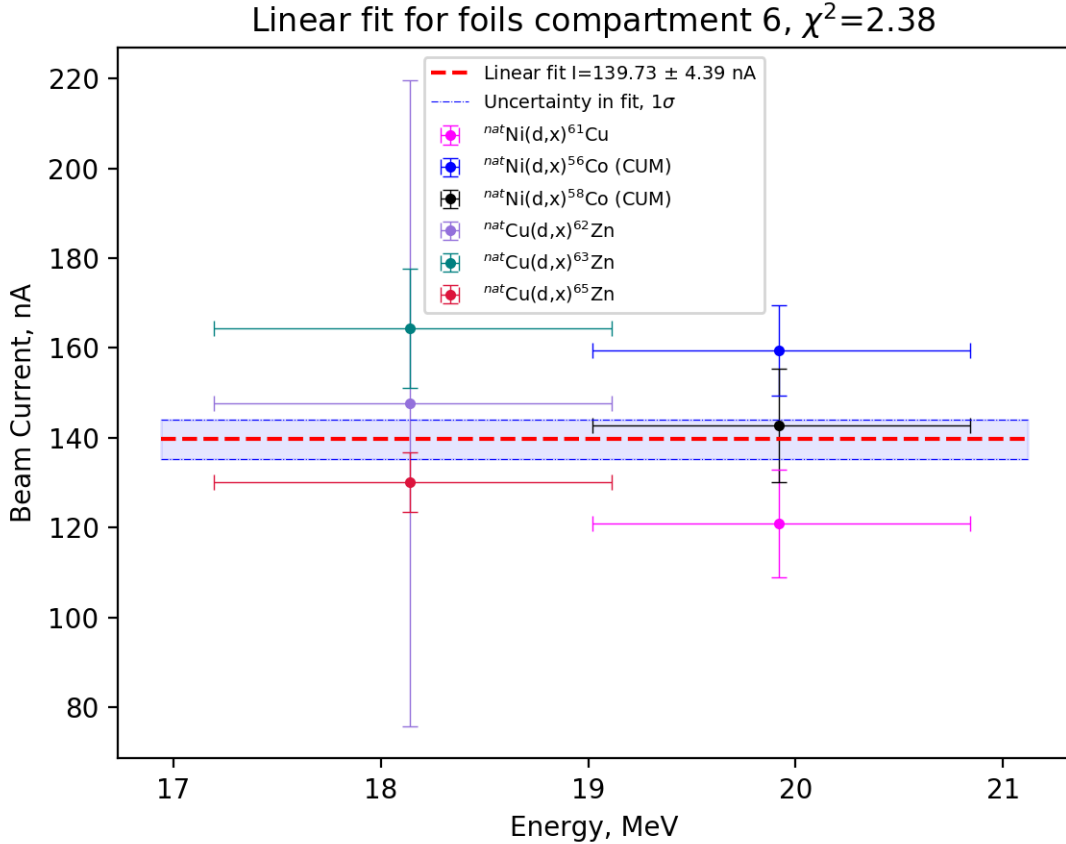


Figure 2.6: The estimated (uncertainty weighted) beamcurrent over compartment 6.

With the assumption that the beamcurrent loss is zero over one compartment, a linear fit-model (using the scipy optimize curvefit function) with a slope equal to zero was used to estimate the beam current in each compartment, and with the estimated χ^2 .

Figure 2.6 shows the uncertainty weighted linear fit over compartment 6.

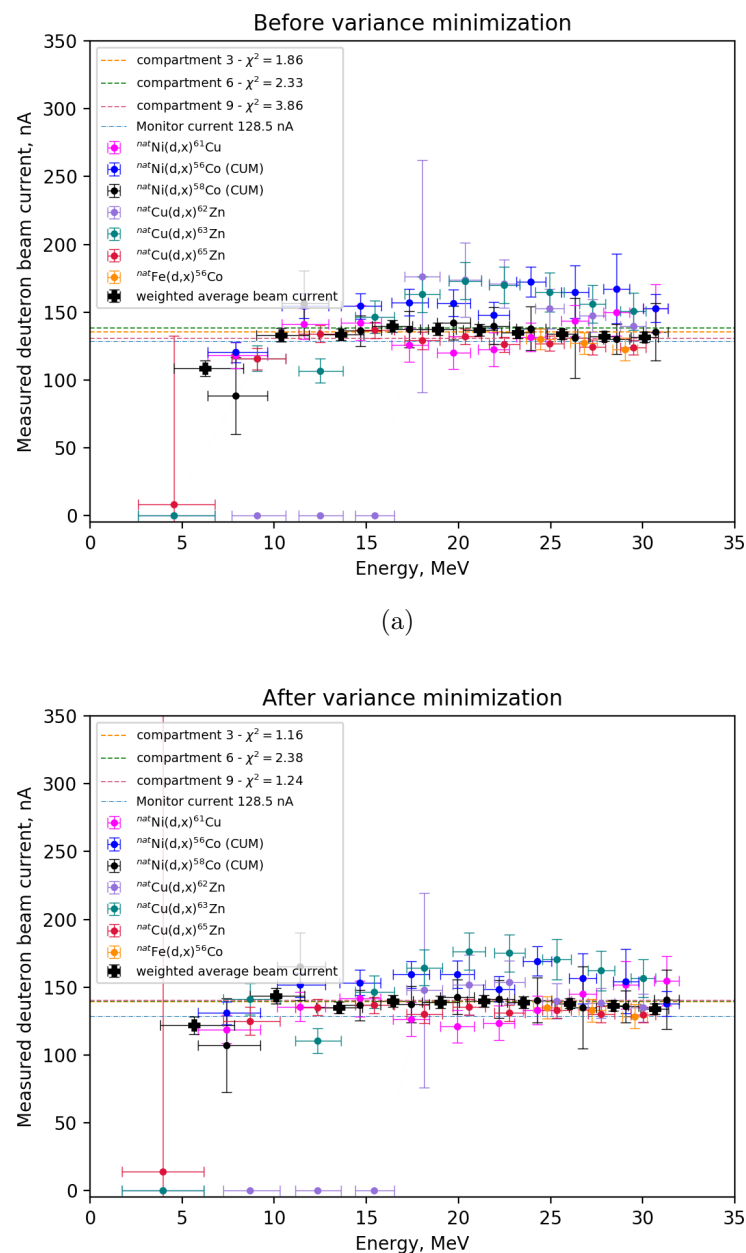
Figure 2.7 shows the beam current before and after variance minimization, and the weighted average beam currents are listed in table 2.1 estimated before and after the variance minimization. After variance minimization, the beam current estimated in each compartment (stabled lines) were similar, and meanwhile the weighted χ^2 was about the same in compartment 6, it has improved in compartment 3 and very visible in compartment 9. In general the points are also more aligned.

2.5 Cross section measurements

With all variables for cross sections, cross sections can be calculated using equation ???. Since the energy was a flux-weighted average beam energy, the value that is provided as cross section is a flux-averaged cross section. An accurate measure of the cross section as a function of deuteron energy was possible, as the thin foils provides smaller average beam energy intervals, and it makes it possible to have more measurements if thick foils are replaced with several thinner (one single foil represents a single measurement). **in theory: Thin foils also produce minimal amounts of radioactivity, thus the deadtime of the detector and the dose to humans is low.**

Thin foils decreases the energy width, making a more precise measurement dependent on energy. However the reported cross sections are flux-averaged over the energy distribution subtended by each foil.

The cross sections are reported as independent if there is nothing decaying into it (beta feeding or from isomer transition), which means that the first observed element in a decay chain is reported



(b) A 2% increase in beam current and a 4.25% increase in areal density gave the overall most consistent beam current, with reasonable values for the weighted .

Figure 2.7: Beam current before and after variance minimization.

Table 2.1: The weighted average beam current before and after variance minimization in each compartment. The beam current on the 88-Inch Cyclotron beam integrator was 128.5 nA.

| Compartment | Before | After |
|-------------|--------------|--------------|
| 01 | 131.56 ±3.64 | 134.08 ±3.70 |
| 02 | 132.23 ±3.74 | 136.42 ±3.83 |
| 03 | 133.81 ±3.64 | 138.02 ±3.75 |
| 04 | 134.89 ±4.21 | 138.88 ±4.31 |
| 05 | 136.85 ±4.21 | 139.67 ±4.29 |
| 06 | 137.40 ±4.53 | 138.85 ±4.58 |
| 07 | 139.55 ±4.37 | 139.77 ±4.37 |
| 08 | 133.60 ±4.27 | 134.96 ±4.32 |
| 09 | 133.16 ±5.04 | 143.59 ±5.67 |
| 10 | 108.49 ±5.80 | 121.75 ±6.65 |

as cumulative unless it is the first possible element (which are the nuclei with one more proton more than the target nuclei, which for this experiment is Platinum (from Ir), Zink (from Cu), Copper (from Ni) and Cobalt (from Fe). If there is feeding, and the half life is much shorter or much longer than the specific nuclei, can choose appropriate timewindow and report as independent, when we know that the feeding has either died out or is very low!

The measured cross sections in this work was compared to previous experimental data, along with reaction modelling codes TALYS^{https://sci-hub.tw/https://doi.org/10.1016/j.nds.2012.11.002}, TENDL, ALICE20 and CoH.

Optical model calculations performed first,

Talys takes in projectile, target element (specific isotope or all stable target isotopes), energy array with desired spacing and upper limit energy.

For COH: To get both 191Ir and 193Ir to run, we had to adjust the parameter "tweakSD", which adjusts the effective single-particle state density for a particular particle emission channel. In the end, we ran with tweakSD=0.25 for both outgoing alphas and neutrons (protons were unaffected). In other words, we set the single-particle state density for outgoing alphas and neutrons [(d,xa) and (d,xn) reactions] to be 25% of what they normally are, which is a HUGE change.

from talys cite p. 2843-2844: TENDL is developed from talys (TALYS evaluated Nuclear data Library). This library consists of a complete set of nuclear reaction data for incident neutrons, photons, protons, deuterons, tritons, Helium-3 and alpha particles, from 10^5 eV up to 200 MeV, for all 2430 isotopes from ^6Li to ^{281}Ds that are either stable or have a half-life longer than 1 second. All data are completely and consistently evaluated using a software system consisting of the TALYS nuclear reaction code, and other software to handle resonance data, experimental data, data from existing evaluations, and to provide the final ENDF-6 formatting, including covariance information. The result is a nuclear data library with mutually consistent reaction information for all isotopes and a quality that increases with yearly updates. To produce this library, TALYS input parameters are adjusted for many nuclides so that calculated cross sections agree with experimental data, while for important nuclides experimental or evaluated data are directly included. Also feedback from integral measurements is processed into the data libraries. For nuclides for which (almost) no experimental data exists, default TALYS calculations based on global models and parameters are used.

Dont understand this part.....

Chapter 3

Statistics

Uncertainty in statistics refers to the standard deviation of the data, which gives a number of the spreading of the data from the mean value of the data citation. The variance is the standard deviation squared, which weights the variables to a higher degree.

$$std = \sqrt{\sigma^2} \quad (3.1)$$

$$\sigma = \sqrt{\frac{1}{N} \sum_{i=1}^N (x_i - \bar{x})^2} \quad (3.2)$$

where N is the number of measurements, x_i is a measurement and \bar{x} is the average over all measurements.

χ^2 is an estimation of the goodness of the fit, which includes the weight of the error

$$\chi^2 = \sum_i^n \left(\frac{y_i - \bar{y}}{\sigma_i} \right)^2 \quad (3.3)$$

where \bar{y} is the mean value of y and σ_i is the error in y_i . The reduced χ^2 is defined as the χ^2 per degree of freedom

$$\chi_\nu^2 = \frac{\chi^2}{\nu} \quad (3.4)$$

where ν is the degrees of freedom equal to the number of observations minus the number of fitted parameters. A value close to $\chi_\nu^2 = 1$ indicates that the observations and fit is in well accordance to the error, while $\chi_\nu^2 > 1$ indicates an underfitting and a $\chi_\nu^2 < 1$ indicates an overfitting¹.

A function f with input x and a set of variables $\vec{\beta} = \beta_1, \beta_2, \dots, \beta_n$ and output y can be written on the following form

$$y = f(x, \vec{\beta}) \quad (3.5)$$

The uncertainty in y is dependent on the uncertainty in the different input variables $\vec{\beta}$. The matrix expression for error propagation is (Tellinghuisen, Joel, Statistical error propagation)²

$$\sigma_y^2 = \mathbf{J} \cdot \mathbf{V} \cdot \mathbf{J}^T \quad (3.6)$$

where σ_y^2 is the variance in y, J is the Jacobian matrix

$$\mathbf{J} = \begin{bmatrix} \frac{\partial f}{\partial \beta_1} & \frac{\partial f}{\partial \beta_2} & \dots & \frac{\partial f}{\partial \beta_n} \end{bmatrix} \quad (3.7)$$

and V is the variance-covariance matrix

¹https://en.wikipedia.org/wiki/Reduced_chi-squared_statistic

²A full derivation of the expression can be found in Uncertainty Propagation for Measurements with multiple output quantities, Dobbert, Schrijver

$$\mathbf{V} = \begin{bmatrix} \sigma_0^2 & \sigma_{0,1} & \cdots & \sigma_{0,n} \\ \sigma_{1,0} & \sigma_1^2 & \cdots & \sigma_{1,n} \\ \vdots & \vdots & \ddots & \vdots \\ \sigma_{n,0} & \sigma_{n,1} & \cdots & \sigma_n^2 \end{bmatrix} \quad (3.8)$$

In the cases where the input parameters are uncorrelated, all non-diagonal elements in the variance-covariance matrix is equal to zero, and the expression for the variance is simplified to

$$\sigma_y^2 = \sum_{i=1}^n \left(\frac{\partial f}{\partial \beta_i} \right)^2 \sigma_{\beta_i}^2 \quad (3.9)$$

Whenever the input parameters are correlated, which means that $\sigma_{\beta_i, \beta_j} \neq 0$, we have to apply equation 3.6, otherwise, the simplification in equation 3.9 will give wrong error propagation.

To evaluate the partial derivatives of f , the computational derivation is applicable

$$\frac{\partial f}{\partial \beta_i} \simeq \frac{f(x, \beta_i + \frac{\Delta \beta_i}{2}) - f(x, \beta_i - \frac{\Delta \beta_i}{2})}{\Delta \beta_i} \quad (3.10)$$

where $\Delta \beta_i$ is a small number, like $10^{-8} \beta_i$.

For a function $f = xy$, the variance can be expressed from equation 3.6, where

$$\mathbf{J} = [y \quad x]$$

and

$$\mathbf{V} = \begin{bmatrix} \sigma_x^2 & \sigma_{x,y} \\ \sigma_{y,x} & \sigma_y^2 \end{bmatrix}$$

$$\sigma_f^2 = x^2 \sigma_y^2 + y^2 \sigma_x^2 + 2xy \sigma_{x,y} \quad (3.11)$$

If we multiply each term so that we can collect f^2 in the numerator, the variance in f can be expressed as

$$\sigma_f^2 = f^2 \left(\frac{\sigma_x^2}{x^2} + \frac{\sigma_y^2}{y^2} + \frac{2\sigma_{x,y}}{xy} \right) \quad (3.12)$$

if the variables x and y are uncorrelated, the variance is further simplified, and more terms can be included easily. The simplified standard deviation of a function $f(\vec{\beta}) = \beta_1 \cdot \beta_2 \cdots \beta_n$ with uncorrelated variables is thus

$$\sigma_f = |f| \sqrt{\left(\frac{\sigma_{\beta_1}}{\beta_1} \right)^2 + \left(\frac{\sigma_{\beta_2}}{\beta_2} \right)^2 + \cdots + \left(\frac{\sigma_{\beta_n}}{\beta_n} \right)^2} \quad (3.13)$$

3.0.1 Radioactive decay law

From here based on Krane chapter 6 ³

The activity of a nucleus is defined as the number of decayed nuclei per unit time of a radioactive product, which is equal to the radioactive decay rate

$$A = \frac{dN}{dt} = -\lambda N \quad (3.14)$$

where N is the number of nuclei, t is the time and λ is the decay constant. Solving equation 3.14 gives number of decayed products at time t

$$N(t) = N_0 e^{-\lambda t} \quad (3.15)$$

³<https://faculty.kfupm.edu.sa/phys/aanaqvi/Krane-Ch-6.pdf>

Since $N \propto A$, the relations $\frac{N_0}{A_0} = \frac{N(t)}{A(t)}$ are valid, and we can rewrite the equation 3.15 to

$$A(t) = A_0 e^{-\lambda t} \quad (3.16)$$

This accounts for single nucleus decaying into a daughter product, without anything first decaying into the parent nucleus. However it is common that a radioactive nucleus decays into another radioactive nucleus. Hence the daughter activity will increase due to feeding from the parent. For multiple decay, Bateman equation is used describing the activity in nucleus n of the decay chain ([Voyles2018, which article??](#))

$$A_n = \lambda_n \sum_{i=1}^n \left[\left(A_{i,0} \prod_{j=i}^{n-1} \lambda_j \right) \cdot \left(\sum_{j=i}^n \frac{e^{-\lambda_j t}}{\prod_{i \neq j}^n (\lambda_i - \lambda_j)} \right) \right] \quad (3.17)$$

where A_n is the activity of nuclei n in the decay chain, with the corresponding decay constant λ_n . The equation sums over all nuclei in the decay chain. $A_{i,0}$ is the initial activity of nucleus i, and j is the nucleus which is feeding into nucleus i.

If a target of stable nuclei is assumed, which is exposed to a particle beam which induces various nuclear reactions, the constant rate of production of a specific reaction is dependent on the number of target nuclei, the current of flux of the particle beam and the reaction cross section

$$R = N_T \Phi \sigma \quad (3.18)$$

where R is the production rate, N_T is the number of target nuclei, Φ is the beam current or flux and σ is the reaction cross section. In the assumption of the production rate being a constant value, the number of transformed target nuclei is small in comparison to the total number during the irradiation time. The number of produced nuclei from a specific reaction per unit time is thus the produced nuclei minus the decayed nuclei (activity)

$$dN = R dt - \lambda N dt \quad (3.19)$$

which has the solution

$$N(t) = \frac{R}{\lambda} (1 - e^{-\lambda t}) \quad (3.20)$$

From equation 3.14, the total activity produced during irradiation time t is thus

$$A(t) = R(1 - e^{-\lambda t}) = N_T \Phi \sigma (1 - e^{-\lambda t}) \quad (3.21)$$

At the end of beam, the activity is denoted as A_0 , and t is the irradiation time:

$$A_0 = N_T \Phi \sigma (1 - e^{-\lambda \Delta t_{\text{irr}}}) \quad (3.22)$$

When a target is irradiated, the activity of the product nucleus will increase until secular equilibrium is achieved, which is when the product rate and decay rate are constant. Hence it is not necessary to irradiate a target for more than 2-3 half lives.

If a spectrum is counted at a delay time Δt_d after end of beam with a counting time Δt_c the total number of decayed products are

$$N_D = \int_{\Delta t_d}^{\Delta t_d + \Delta t_c} A(t) dt \quad (3.23)$$

Using equation 3.16 for $A(t)$, the solution to the above equation is

$$N_D = \frac{A_0}{\lambda} e^{-\lambda \Delta t_d} (1 - e^{-\lambda \Delta t_c}) \quad (3.24)$$

which again is equal to

$$N_D = \frac{A(t)}{\lambda} (1 - e^{-\lambda \Delta t_c}) \quad (3.25)$$

We can only know the number of decayed products which are detected. This is dependent on the efficiency of the detector, the intensity of the gamma-rays and the true number of decayed products

$$N_C = N_D \epsilon I_\gamma \quad (3.26)$$

where N_C is the number of observed/counted gamma-rays, ϵ is the efficiency of the detector and I_γ is the gamma-ray intensity.

Thus, we can obtain an expression for $A(t)$ after a delay time:

$$A(t) = \frac{N_C \lambda}{\epsilon I_\gamma (1 - e^{-\lambda \Delta t_c})} \quad (3.27)$$

Again using 3.16 for $A(t)$, the above expression can be rewritten using A_0 and the delay time Δt_d

$$A_0 = \frac{N_C \lambda}{\epsilon I_\gamma (1 - e^{-\lambda \Delta t_c}) e^{-\lambda \Delta t_d}} \quad (3.28)$$

Chapter 4

Tables

For all tables, the assumption is that the main particle emission is due to alpha, proton or neutron emission. However, triton, ^3He and deuterons are still fed when above threshold, but from theory, the feeding is low. For triton, ^3He and deuteron respectively, subtract 8.5, 7.7 or 2.2 respectively from the Q value. Alphaparticles (due to the large binding energy and spin equal to 0) will be more fed. To calculate Q value for alpha emission subtract 28.3 MeV from Q value of 2p2n-reactions. Q values from ¹ are used. Q values below 40 MeV are included for comparison to experimental data.

4.1 Product nuclei, Q-values and gammarays

Table 4.1: Products observed on Nickel foils. Nickel has five stable isotopes: ^{58}Ni (68.077%), ^{60}Ni (26.223 %), ^{61}Ni (1.1399%), ^{62}Ni (3.6346%) and ^{64}Ni (0.9255%). If the nucleus has provided energy level, the nucleus is an isomer, if nothing then ground state. The table is inspired by Tarkanyi et al 2019 (in paper)

| Nuclide level (keV) | Half life | Decay mode | Reaction route | Q value (keV) | E_γ (keV) | I_γ (%) |
|---------------------------|-------------------|-------------------|--|---------------|------------------|----------------|
| ^{52}Mn (0.0) | 5.591 d 21.1 m | ϵ : 100% | $^{58}\text{Ni}(\text{d},2\alpha)$ | -1235.6 | 744.233 | 90.0 |
| | | | $^{60}\text{Ni}(\text{d},2\text{n}2\alpha)$ | -21622.6 | 935.544 | 94.5 |
| | | | $^{61}\text{Ni}(\text{d},3\text{n}2\alpha)$ | -29442.7 | 1246.278 | 4.21 |
| | | | | | 1434.092 | 100.0 |
| ^{54}Mn (0.0) | 312.20 d | ϵ : 100% | $^{58}\text{Ni}(\text{d},2\text{p}\alpha)$ | -8538.3 | 834.848 | 99.9760 |
| | | | $^{60}\text{Ni}(\text{d},2\alpha)$ | -629.6 | | |
| | | | $^{61}\text{Ni}(\text{d},\text{n}2\alpha)$ | -8449.7 | | |
| | | | $^{62}\text{Ni}(\text{d},2\text{n}2\alpha)$ | -19045.4 | | |
| ^{59}Fe (0.0) | 44.490 d | β^- : 100% | $^{60}\text{Ni}(\text{d},3\text{p})$ | -12539.5 | 1291.590 | 43.2 |
| | | | $^{61}\text{Ni}(\text{d},\text{n}3\text{p})$ | -20359.6 | | |
| | | | $^{62}\text{Ni}(\text{d},\text{p}\alpha)$ | -2659.7 | | |
| | | | $^{64}\text{Ni}(\text{d},2\text{n}\text{p}\alpha)$ | -19154.9 | | |

¹<https://www.nndc.bnl.gov/qcalc/>

| | | | | | | |
|---------------------------|-----------|--------------------|--|--|---|--|
| ^{55}Co (0.0) | 17.53 h | $\epsilon : 100\%$ | $^{58}\text{Ni}(\text{d},\text{n}\alpha)$ $^{60}\text{Ni}(\text{d},3\text{n}\alpha)$ $^{61}\text{Ni}(\text{d},4\text{n}\alpha)$ | -3559.4 -23946.4 -31766.5 | 91.9 385.4 477.2 520.0 803.7 827.0 931.1 984.6 1212.8 1316.6 1370.0 1408.5 1792.1 2177.6 2872.4 | 1.16 0.54 20.2 0.83 1.87 0.21 75 0.52 0.26 7.1 2.9 16.9 0.082 0.29 0.118 |
| ^{56}Co (0.0) | 77.236 d | $\epsilon : 100\%$ | $^{58}\text{Ni}(\text{d},\alpha)$ $^{61}\text{Ni}(\text{d},2\text{n}\alpha)$ $^{61}\text{Ni}(\text{d},3\text{n}\alpha)$ $^{62}\text{Ni}(\text{d},4\text{n}\alpha)$ | 6522.5 -13864.5 -21684.6 -32280.4 | 787.743 846.770 977.372 1175.101 1963.741 2015.215 2034.791 | 0.3111 99.9399 1.421 2.252 0.707 3.016 7.77 |
| ^{58}Co (0.0) | 70.86 d | $\epsilon : 100\%$ | $^{58}\text{Ni}(\text{d},2\text{n})$ $^{60}\text{Ni}(\text{d},\alpha)$ $^{61}\text{Ni}(\text{d},\text{n}\alpha)$ $^{62}\text{Ni}(\text{d},2\text{n}\alpha)$ $^{64}\text{Ni}(\text{d},4\text{n}\alpha)$ | -1823.8 6084.9 -1735.3 -12331.0 -28826.2 | 810.7593 863.951 1674.725 | 99.450 0.686 0.517 |
| ^{60}Co (0.0) | 1925.28 d | $\beta^- : 100\%$ | $^{60}\text{Ni}(\text{d},2\text{p})$ $^{61}\text{Ni}(\text{d},\text{n}2\text{p})$ $^{62}\text{Ni}(\text{d},\alpha)$ $^{64}\text{Ni}(\text{d},2\text{n}\alpha)$ | -4265.0 -12085.1 5614.8 -10880.4 | 1173.228 1332.492 | 99.85 99.9826 |
| ^{56}Ni (0.0) | 6.075 d | $\epsilon : 100\%$ | $^{58}\text{Ni}(\text{d},3\text{np})$ | -24688.4 | 158.38 480.44 749.95 811.85 1561.80 | 98.8 36.5 49.5 86.0 14.0 |
| ^{57}Ni (0.0) | 35.60 h | $\beta^+ : 100\%$ | $^{58}\text{Ni}(\text{d},2\text{np})$ $^{60}\text{Ni}(\text{d},4\text{np})$ | -14440.8 -34827.8 | 379.94 673.44 906.98 1046.68 1224.00 1377.63 1730.44 1757.55 1897.42 1919.52 2133.04 2804.20 | 0.0670 0.0491 0.0613 0.134 0.063 81.7 0.052 5.75 0.028 12.3 0.0286 0.098 |
| ^{65}Ni (0.0) | 2.51719 h | $\beta^- : 100\%$ | $^{64}\text{Ni}(\text{d},\text{p})$ | 3873.51 | 366.27 1481.84 1623.42 1724.92 | 4.81 23.59 0.498 0.399 |

| | | | | | | |
|---------------------------|----------|--|---|---|---|---|
| ^{60}Cu (0.0) | 23.7 m | $\epsilon : 100\%$ | $^{60}\text{Ni}(\text{d},2\text{n})$ $^{61}\text{Ni}(\text{d},3\text{n})$ $^{62}\text{Ni}(\text{d},4\text{n})$ | -9134.9 -16955.0 -27550.7 | 467.3 497.9 643.2 952.4 1035.2 1110.5 1293.7 1791.6 1861.6 1936.9 2061.0 2158.9 2403.3 2687.9 2746.1 | 3.52 1.67 0.97 2.73 3.70 1.06 1.85 45.4 4.8 2.20 0.79 3.34 0.77 0.44 1.06 |
| ^{61}Cu | 3.339 h | $\epsilon : 100\%$ | $^{60}\text{Ni}(\text{d},\text{n})$ $^{61}\text{Ni}(\text{d},2\text{n})$ $^{62}\text{Ni}(\text{d},3\text{n})$ $^{64}\text{Ni}(\text{d},5\text{n})$ | 2575.3 -5244.8 -15840.5 -32335.7 | 282.956 373.050 529.169 588.605 625.605 656.008 816.692 841.211 902.294 1032.162 1073.465 1132.351 1185.234 1446.492 | 12.2 2.1 0.38 1.17 0.040 10.8 0.31 0.21 0.083 0.043 0.033 0.090 3.7 0.045 |
| ^{64}Cu | 12.701 h | $\epsilon : 100\%$ $\beta^- : 38.5\%$ | $^{64}\text{Ni}(\text{d},2\text{n})$ | -4681.3 | 1345.77 | 0.475 |

Table 4.2: Products observed on Iron foils. Iron has five stable isotopes: ^{54}Fe (5.845%), ^{56}Fe (91.754 %), ^{57}Fe (2.119%) and ^{58}Fe (0.282%). If the nucleus has provided energy level, the nucleus is an isomer, if nothing then ground state. **The table is inspired by Tarkanyi et al 2019 (ir paper)**

| Nuclide level (keV) | Half life | Decay mode | Reaction route | Q value (keV) | E_γ (keV) | I_γ (%) |
|---------------------------|-------------|--------------------|---|---------------|------------------|----------------|
| ^{48}V (0.0) | 15.9735 d | $\epsilon : 100\%$ | $^{54}\text{Fe}(\text{d},2\alpha)$ | -3490.9 | 944.130 | 7.870 |
| | | | $^{56}\text{Fe}(\text{d},2\text{n}2\alpha)$ | -23986.1 | 983.525 | 99.98 |
| | | | $^{57}\text{Fe}(\text{d},3\text{n}2\alpha)$ | | 1312.106 | 98.2 |
| ^{51}Cr (0.0) | 27.704 d | $\epsilon : 100\%$ | $^{54}\text{Fe}(\text{d},\text{p}\alpha)$ | -1381.3 | 320.0824 | 9.910 |
| | | | $^{56}\text{Fe}(\text{d},2\text{n}\alpha)$ | -21876.5 | | |
| | | | $^{57}\text{Fe}(\text{d},3\text{n}\alpha)$ | -29522.6 | | |
| | | | $^{58}\text{Fe}(\text{d},4\text{n}\alpha)$ | -39567.2 | | |
| ^{52}Mn (0.0) | 5.591 d d | $\epsilon : 100\%$ | $^{54}\text{Fe}(\text{d},\alpha)$ | 5163.6 | 346.02 | 0.980 |
| | | | $^{56}\text{Fe}(\text{d},2\text{n}\alpha)$ | -15331.6 | 744.233 | 90.0 |
| | | | $^{57}\text{Fe}(\text{d},3\text{n}\alpha)$ | -22977.7 | 848.18 | 3.32 |
| | | | | | 935.544 | 94.5 |
| | | | | | 1246.278 | 4.21 |
| | | | | | 1333.649 | 5.07 |
| | | | | | 1434.092 | 100.0 |
| ^{54}Mn (0.0) | 312.20 d | $\epsilon : 100\%$ | $^{54}\text{Fe}(\text{d},2\text{p})$ | -2139.1 | 834.8480 | 99.9760 |
| | | | $^{56}\text{Fe}(\text{d},\alpha)$ | 5661.4 | | |
| | | | $^{57}\text{Fe}(\text{d},\text{n}\alpha)$ | -1984.7 | | |
| | | | $^{58}\text{Fe}(\text{d},2\text{n}\alpha)$ | -12029.3 | | |
| ^{53}Fe (0.0) | 8.51 m ???? | $\epsilon : 100\%$ | $^{54}\text{Fe}(\text{d},2\text{np})$ | -15602.9 | 377.9 | 42% |
| | | | $^{56}\text{Fe}(\text{d},4\text{np})$ | -36098.1 | | |
| ^{59}Fe (0.0) | 44.490 d | $\beta^- : 100\%$ | $^{58}\text{Fe}(\text{d},\text{p})$ | 4356.44 | 1099.245 | 56.5 |
| | | | | | 1291.590 | 43.2 |
| ^{55}Co (0.0) | 17.53 h | $\epsilon : 100\%$ | $^{54}\text{Fe}(\text{d},\text{n})$ | 2839.8 | 91.9 | 1.16 |
| | | | $^{56}\text{Fe}(\text{d},3\text{n})$ | -17655.4 | 477.2 | 20.2 |
| | | | $^{57}\text{Fe}(\text{d},4\text{n})$ | -25301.5 | 803.7 | 1.87 |
| | | | | | 827.0 | 0.21 |
| | | | | | 931.1 | 75 |
| | | | | | 1316.6 | 7.1 |
| | | | | | 1370.0 | 2.9 |
| | | | | | 1408.5 | 16.9 |
| | | | | | 2177.6 | 0.29 |
| | | | | | 2872.4 | 0.118 |
| | | | | | 2938.9 | 0.057 |

| | | | | | | |
|------------------|----------|--------------------|--------------------------------------|----------|-----------|---------|
| ^{56}Co | 77.236 d | $\epsilon : 100\%$ | $^{56}\text{Fe}(\text{d},2\text{n})$ | -7573 | 263.434 | 0.0220 |
| (0.0) | | | $^{57}\text{Fe}(\text{d},3\text{n})$ | -15219.7 | 486.55 | 0.0540 |
| | | | $^{58}\text{Fe}(\text{d},4\text{n})$ | -25264.3 | 733.514 | 0.191 |
| | | | | | 787.743 | 0.311 |
| | | | | | 846.770 | 99.9399 |
| | | | | | 852.732 | 0.049 |
| | | | | | 896.510 | 0.073 |
| | | | | | 977.372 | 1.421 |
| | | | | | 996.948 | 0.111 |
| | | | | | 1037.843 | 14.05 |
| | | | | | 1140.368 | 0.132 |
| | | | | | 1159.944 | 0.094 |
| | | | | | 1175.101 | 2.252 |
| | | | | | 1198.888 | 0.049 |
| | | | | | 1238.288 | 66.46 |
| | | | | | 1335.40 | 0.1224 |
| | | | | | 1360.212 | 4.283 |
| | | | | | 1771.357 | 15.41 |
| | | | | | 1963.741 | 0.707 |
| | | | | | 2015.215 | 3.016 |
| | | | | | 2034.791 | 7.77 |
| | | | | | 2212.944 | 0.388 |
| | | | | | 2276.131 | 0.118 |
| | | | | | 2598.500 | 16.97 |
| ^{57}Co | 271.74 d | $\epsilon : 100\%$ | $^{56}\text{Fe}(\text{d},\text{n})$ | 3802.9 | 122.06065 | 85.60 |
| (0.0) | | | $^{57}\text{Fe}(\text{d},2\text{n})$ | -3843.2 | 136.47356 | 10.68 |
| | | | $^{58}\text{Fe}(\text{d},3\text{n})$ | -13887.8 | | |
| ^{58}Co | 70.86 | $\epsilon : 100\%$ | $^{57}\text{Fe}(\text{d},\text{n})$ | 4729.7 | 810.7593 | 99.450 |
| (0.0) | | | $^{58}\text{Fe}(\text{d},2\text{n})$ | -5314.9 | | |

Table 4.3: Products observed on Copper foils. Copper has two stable isotopes: ^{63}Cu (69.15%) and ^{65}Cu (30.85 %). If the nucleus has provided energy level, the nucleus is an isomer, if nothing then ground state. **The table is inspired by Tarkanyi et al 2019 (in paper)**

| Nuclide level (keV) | Half life | Decay mode | Reaction route | Q value (keV) | E_{γ} (keV) | I_{γ} (%) |
|---------------------------|-----------|--|--|---------------|--------------------|------------------|
| ^{59}Fe (0.0) | 44.490 d | β^- : 100% | $^{63}\text{Cu}(\text{d},2\text{p}\alpha)$ | -8782.1 | 1099.245 | 56.5 |
| | | | $^{65}\text{Cu}(\text{d},2\alpha)$ | 1687.0 | 1291.590 | 43.2 |
| ^{60}Co (0.0) | 1925.28 d | β^- : 100% | $^{63}\text{Cu}(\text{d},\text{p}\alpha)$ | -507.6 | 1173.228 | 99.85 |
| | | | $^{65}\text{Cu}(\text{d},\text{t}\alpha)$ | -9852.4 | 1332.492 | 99.9826 |
| ^{61}Co (0.0) | 1.649 h | β^- : 100% | $^{63}\text{Cu}(\text{d},\text{n}3\text{p})$ | -19484.2 | 67.412 | 84.7 |
| | | | $^{65}\text{Cu}(\text{d},\text{np}\alpha)$ | -9015.1 | | |
| ^{65}Ni (0.0) | 2.51719 h | β^- : 100% | $^{65}\text{Cu}(\text{d},2\text{p})$ | -3580.2 | 1481.84 | 23.59 |
| | | | $^{63}\text{Cu}(\text{d},3\text{np})$ | -21962.9 | 282.956 | 12.2 |
| ^{61}Cu (0.0) | 3.339 h | ϵ : 100% β^- : 38.5 | $^{65}\text{Cu}(\text{d},5\text{np})$ | -39789.4 | 656.008 | 10.8 |
| | | | $^{63}\text{Cu}(\text{d},\text{p})$ | 5691.54 | 1185.234 | 3.7 |
| ^{64}Cu (0.0) | 12.701 h | ϵ : 61.5% β^- : 38.5 | $^{65}\text{Cu}(\text{d},2\text{np})$ | -12135.0 | 1345.77 | 0.475 |
| | | | $^{63}\text{Zn}(\text{d},3\text{n})$ | -15490.0 | 40.85 | 25.5 |
| ^{62}Zn (0.0) | 9.193 h | ϵ : 100% | $^{65}\text{Cu}(\text{d},5\text{n})$ | -33316.6 | 243.36 | 2.52 |
| | | | | | 246.95 | 1.90 |
| | | | | | 260.43 | 1.35 |
| | | | | | 304.88 | 0.29 |
| | | | | | 394.03 | 2.24 |
| | | | | | 548.35 | 15.3 |
| | | | | | 596.56 | 26.0 |
| ^{63}Zn (0.0) | 38.47 m | ϵ : 100% | | | 637.41 | 0.25 |
| | | | $^{63}\text{Cu}(\text{d},2\text{n})$ | -6373.3 | 449.93 | 0.236 |
| | | | $^{65}\text{Cu}(\text{d},4\text{n})$ | -24199.8 | 669.62 | 8.2 |
| ^{65}Zn (0.0) | 243.93 d | ϵ : 100% | | | 962.06 | 6.5 |
| | | | $^{65}\text{Cu}(\text{d},2\text{n})$ | -4358.6 | 1115.539 | 50.04 |

Table 4.4: Products observed in Iridium foils. Iridium has two stable isotopes: ^{191}Ir (37.3%) and ^{93}Ir (62.7 %). If the nucleus has provided energy level, the nucleus is an isomer, if nothing then ground state. **The table is inspired by Tarkanyi et al 2019 (ir paper)**

| Nuclide level (keV) | Half life | Decay mode | Reaction route | Q value (keV) | E_γ (keV) | I_γ (%) |
|---------------------------------|-----------|--|--|---------------|------------------|----------------|
| ^{188}Ir (0.0) | 41.5 h | ϵ : 100% | $^{191}\text{Ir}(\text{d},4\text{np})$ | -24802.0 | 1209.80 | 6.9 |
| | | | | | 1715.67 | 6.2 |
| | | | | | 2059.65 | 7.0 |
| ^{189}Ir (0.0) | 13.2 d | ϵ : 100% | $^{191}\text{Ir}(\text{d},4\text{np})$ | -16626.0 | 95.23 | 0.38 |
| | | | | -30596.0 | 216.7 | 0.52 |
| | | | $^{193}\text{Ir}(\text{d},5\text{np})$ | | 233.5 | 0.30 |
| | | | | | 245.1 | 6.0 |
| ^{190}Ir (0.0) | 11.78 d | ϵ : 100% | $^{191}\text{Ir}(\text{d},2\text{np})$ | -10251.1 | 294.75 | 6.6 |
| | | | | -24221.2 | 380.03 | 2.03 |
| | | | | | 1036.05 | 2.42 |
| $^{190m^2}\text{Ir}$ (376.4) | 3.087 h | IT:8.6% ϵ : 91.4% | .. | .. | 361.2 | 86.72 |
| | | | | | 502.5 | 89.38 |
| | | | | | 616.5 | 90.14 |
| ^{192}Ir (0.0) | 73.829 d | ϵ : 4.76% β^- : 95.24% | $^{191}\text{Ir}(\text{d},\text{p})$ | 3973.55 | 201.3112 | 0.471 |
| | | | | -9996.6 | 295.95650 | 28.71 |
| | | | $^{193}\text{Ir}(\text{d},2\text{np})$ | | 374.4852 | 0.727 |
| | | | | | 416.4688 | 0.670 |
| | | | | | 468.06885 | 47.84 |
| | | | | | 489.06 | 0.438 |
| | | | | | 612.46215 | 5.34 |
| | | | | | 1061.49 | 0.0531 |
| ^{194}Ir (0.0) | 19.28 h | β^- : 100% | $^{194}\text{Ir}(\text{d},\text{p})$ | 3842.22 | 293.541 | 2.5 |
| | | | | | 300.741 | 0.35 |
| | | | | | 589.179 | 0.140 |
| | | | | | 938.69 | 0.60 |
| | | | | | 1150.75 | 0.60 |
| | | | | | 1468.91 | 0.19 |
| $^{194m^2}\text{Ir}$ (190+X) | 171 d | β^- : 100% | .. | .. | 338.8 | 55 |
| | | | | | 482.6 | 97 |
| | | | | | 562.4 | 35 |
| | | | | | 687.8 | 3.6 |
| | | | | | | |
| ^{188}Pt (0.0) | 10.16 d | ϵ : 99.999974% α : $2.6E - 5\%$ | $^{191}\text{Pt}(\text{d},2\text{n})$ | -26109.0 | 195.05 | 18.4 |
| | | | | | 381.43 | 7.4 |
| ^{189}Pt (0.0) | 10.87 h | ϵ : 100% | $^{191}\text{Ir}(\text{d},4\text{n})$ | -19389.0 | 94.34 | 6.5 |
| | | | | | 113.82 | 2.5 |
| | | | | | 243.50 | 5.9 |
| | | | | | 317.65 | 2.8 |
| | | | | | 721.38 | 7.9 |
| | | | | | | |
| ^{191}Pt (0.0) | 2.802 d | ϵ : 100% | $^{191}\text{Ir}(\text{d},2\text{n})$ | -4017.0 | 178.96 | 12.5 |
| | | | | -17988.0 | 351.17 | 42.6 |
| | | | $^{193}\text{Ir}(\text{d},4\text{n})$ | | 409.44 | 100 |
| | | | | | 456.47 | 42 |
| | | | | | 538.87 | 181 |
| | | | | | 624.06 | 18.5 |
| ^{193m}Pt (149.783) | 4.33 d | IT:100% | $^{193}\text{Ir}(\text{d},2\text{n})$ | -3063.5 | 66.831 | 7.21 |
| | | | | | 135.5 | 0.1145475 |

Table 4.5: Iridium production cross sections produced from Iridium

| E_d (MeV) | Production cross section (mb) for iridium radionuclides | | | | |
|--------------------------|---|------------------------------------|--------------------------------|------------------------------------|------------------------------------|
| | $^{188m1+g}\text{Ir}_{\text{cum}}$ | $^{188m1+g}\text{Ir}_{\text{ind}}$ | $^{189}\text{Ir}_{\text{cum}}$ | $^{190m1+g}\text{Ir}_{\text{cum}}$ | $^{190m1+g}\text{Ir}_{\text{ind}}$ |
| 30.65 $^{+0.76}_{-0.75}$ | 1.37 \pm 0.10 | 0.42 \pm 0.03 | 332.49 \pm 24.20 | 86.65 \pm 2.89 | 85.88 \pm 2.86 |
| 28.40 $^{+0.80}_{-0.79}$ | 0.45 \pm 0.07 | 0.17 \pm 0.02 | 237.84 \pm 17.44 | 62.80 \pm 2.14 | 62.36 \pm 2.13 |
| 26.03 $^{+0.82}_{-0.82}$ | 0.34 \pm 0.08 | 0.17 \pm 0.03 | 91.49 \pm 5.47 | 44.26 \pm 1.47 | 44.01 \pm 1.46 |
| 23.54 $^{+0.88}_{-0.87}$ | - | - | 19.23 \pm 2.65 | 27.29 \pm 1.02 | 27.19 \pm 1.02 |
| 21.38 $^{+0.94}_{-0.92}$ | - | - | - | 18.73 \pm 0.71 | 18.69 \pm 0.70 |
| 19.03 $^{+1.00}_{-0.99}$ | - | - | - | 14.02 \pm 0.55 | 14.00 \pm 0.55 |
| 16.43 $^{+1.11}_{-1.08}$ | - | - | - | 12.40 \pm 0.51 | 12.39 \pm 0.51 |
| 13.51 $^{+1.28}_{-1.22}$ | - | - | - | 8.26 \pm 0.43 | 8.25 \pm 0.42 |
| 10.09 $^{+1.55}_{-1.41}$ | - | - | - | - | - |
| 5.63 $^{+2.21}_{-1.83}$ | - | - | - | - | - |

Table 4.6: Iridium production cross sections produced from Iridium

| E_d (MeV) | Production cross section (mb) for iridium radionuclides | | | |
|--------------------------|---|--------------------------------|---------------------------------|----------------------------------|
| | $^{190m2}\text{Ir}_{\text{ind}}$ | $^{192}\text{Ir}_{\text{cum}}$ | $^{194g}\text{Ir}_{\text{cum}}$ | $^{194m2}\text{Ir}_{\text{ind}}$ |
| 30.65 $^{+0.76}_{-0.75}$ | 8.87 \pm 0.25 | 188.43 \pm 5.27 | 50.92 \pm 2.18 | - |
| 28.40 $^{+0.80}_{-0.79}$ | 5.03 \pm 0.15 | 152.55 \pm 4.39 | 51.39 \pm 2.89 | - |
| 26.03 $^{+0.82}_{-0.82}$ | 2.92 \pm 0.08 | 124.33 \pm 3.42 | 61.37 \pm 2.39 | 0.74 \pm 0.17 |
| 23.54 $^{+0.88}_{-0.87}$ | 1.16 \pm 0.04 | 100.03 \pm 3.14 | 69.68 \pm 2.76 | 0.68 \pm 0.26 |
| 21.38 $^{+0.94}_{-0.92}$ | 0.45 \pm 0.01 | 90.41 \pm 2.80 | 86.38 \pm 3.18 | 0.65 \pm 0.13 |
| 19.03 $^{+1.00}_{-0.99}$ | 0.16 \pm 0.01 | 90.65 \pm 3.01 | 97.79 \pm 3.99 | 0.60 \pm 0.14 |
| 16.43 $^{+1.11}_{-1.08}$ | 0.06 0.00 | 99.61 \pm 3.14 | 121.54 \pm 4.54 | 0.50 \pm 0.09 |
| 13.51 $^{+1.28}_{-1.22}$ | 0.03 \pm 0.00 | 107.41 \pm 3.48 | 143.27 \pm 5.52 | - |
| 10.09 $^{+1.55}_{-1.41}$ | 0.02 \pm 0.00 | 64.27 \pm 2.56 | 92.78 \pm 4.21 | - |
| 5.63 $^{+2.21}_{-1.83}$ | 0.02 \pm 0.00 | 6.67 \pm 0.37 | 6.32 \pm 0.42 | - |

4.2 Production cross sections

4.2.1 ${}^{\text{nat}}\text{Ir}(\text{d},\text{x})$

Table 4.7: Platinum production cross sections produced from Iridium

| E_d (MeV) | Production cross section (mb) for platinum radionuclides | | | |
|-------------------------|--|--------------------------------|--------------------------------|---------------------------------|
| | $^{188}\text{Pt}_{\text{ind}}$ | $^{189}\text{Pt}_{\text{ind}}$ | $^{191}\text{Pt}_{\text{ind}}$ | $^{193m}\text{Pt}_{\text{ind}}$ |
| $30.65^{+0.76}_{-0.75}$ | 0.94 ± 0.13 | 486.47 ± 21.86 | 597.10 ± 16.55 | 48.11 ± 6.33 |
| $28.40^{+0.80}_{-0.79}$ | 0.30 ± 0.09 | 341.24 ± 16.64 | 483.60 ± 13.79 | 46.78 ± 2.19 |
| $26.03^{+0.82}_{-0.82}$ | 0.17 ± 0.05 | 172.11 ± 8.03 | 353.99 ± 9.67 | 55.68 ± 2.17 |
| $23.54^{+0.88}_{-0.87}$ | - | 30.72 ± 1.48 | 165.12 ± 5.15 | 51.79 ± 2.12 |
| $21.38^{+0.94}_{-0.92}$ | - | 1.04 ± 0.07 | 71.05 ± 2.19 | 58.31 ± 1.96 |
| $19.03^{+1.00}_{-0.99}$ | - | 0.09 ± 0.02 | 77.53 ± 2.57 | 77.98 ± 2.89 |
| $16.43^{+1.11}_{-1.08}$ | - | - | 128.24 ± 4.03 | 115.33 ± 4.09 |
| $13.51^{+1.28}_{-1.22}$ | - | - | 137.37 ± 4.42 | 148.98 ± 5.54 |
| $10.09^{+1.55}_{-1.41}$ | - | - | 53.45 ± 2.12 | 56.18 ± 2.85 |
| $5.63^{+2.21}_{-1.83}$ | - | - | 1.05 ± 0.06 | 1.56 ± 0.12 |

Table 4.8:

| E_d (MeV) | Production cross section (mb) for ... | | | | |
|-------------------------|---------------------------------------|-------------------------------|-------------------------------|-------------------------------|-------------------------------|
| | $^{48}\text{V}_{\text{cum}}$ | $^{51}\text{Cr}_{\text{cum}}$ | $^{52}\text{Mn}_{\text{cum}}$ | $^{54}\text{Mn}_{\text{ind}}$ | $^{53}\text{Fe}_{\text{cum}}$ |
| $29.57^{+0.68}_{-0.68}$ | 0.12 ± 0.01 | 7.54 ± 0.23 | 16.00 ± 0.36 | 23.85 ± 0.70 | 5.12 ± 0.65 |
| $27.26^{+0.73}_{-0.72}$ | 0.09 ± 0.01 | 7.86 ± 0.25 | 5.48 ± 0.16 | 24.18 ± 0.72 | 2.77 ± 0.44 |
| $24.80^{+0.77}_{-0.76}$ | 0.06 ± 0.00 | 8.51 ± 0.29 | 0.91 ± 0.03 | 26.12 ± 0.79 | 1.29 ± 0.30 |

Table 4.9:

| E_d (MeV) | Production cross section (mb) for ... | | | |
|-------------------------|---------------------------------------|-------------------------------|-------------------------------|-------------------------------|
| | $^{59}\text{Fe}_{\text{ind}}$ | $^{55}\text{Co}_{\text{ind}}$ | $^{57}\text{Co}_{\text{ind}}$ | $^{58}\text{Co}_{\text{ind}}$ |
| 0.16 ± 0.02 | 27.15 ± 0.80 | 35.91 ± 1.06 | 1.50 ± 0.05 | $29.57^{+0.68}_{-0.68}$ |
| $27.26^{+0.73}_{-0.72}$ | 0.15 ± 0.02 | 20.44 ± 0.60 | 38.37 ± 1.13 | 1.62 ± 0.05 |
| $24.80^{+0.77}_{-0.76}$ | 0.18 ± 0.04 | 13.82 ± 0.40 | 42.63 ± 1.27 | 2.05 ± 0.07 |

Table 4.10:

| E_d (MeV) | Production cross section (mb) for ... | | | | | |
|-------------------------|---------------------------------------|-------------------------------|-------------------------------|-------------------------------|-------------------------------|-------------------------------|
| | $^{59}\text{Fe}_{\text{cum}}$ | $^{60}\text{Co}_{\text{cum}}$ | $^{61}\text{Co}_{\text{cum}}$ | $^{65}\text{Ni}_{\text{ind}}$ | $^{61}\text{Cu}_{\text{cum}}$ | $^{64}\text{Cu}_{\text{ind}}$ |
| $30.03_{-0.67}^{+0.67}$ | 0.21 ± 0.03 | 9.49 ± 0.52 | 1.62 ± 0.09 | 3.42 ± 1.76 | 4.54 ± 0.87 | 170.76 ± 7.76 |
| $27.74_{-0.71}^{+0.72}$ | 0.18 ± 0.02 | 11.38 ± 0.51 | 0.82 ± 0.07 | 3.84 ± 1.94 | 2.07 ± 0.95 | 153.78 ± 8.20 |
| $25.32_{-0.76}^{+0.77}$ | 0.17 ± 0.02 | 12.02 ± 0.51 | 0.29 ± 0.05 | 2.89 ± 1.48 | $1.18 \text{ pm } 0.72$ | 132.56 ± 6.93 |
| $22.77_{-0.81}^{+0.83}$ | 0.12 ± 0.01 | 11.36 ± 0.43 | - | 1.92 ± 1.14 | - | 121.54 ± 7.12 |
| $20.57_{-0.87}^{+0.89}$ | 0.07 ± 0.01 | 9.27 ± 0.41 | - | - | - | 106.07 ± 5.81 |
| $18.14_{-0.94}^{+0.97}$ | 0.03 ± 0.01 | 5.65 ± 0.26 | - | 1.46 ± 0.95 | - | 95.92 ± 7.14 |
| $15.43_{-1.04}^{+1.08}$ | - | 1.53 ± 0.12 | - | - | - | 123.79 ± 6.62 |
| $12.34_{-1.20}^{+1.27}$ | - | - | - | - | - | 156.65 ± 8.20 |
| $8.68_{-1.43}^{+1.62}$ | - | - | - | - | - | 209.38 ± 11.27 |
| $3.94_{-2.22}^{+2.25}$ | - | - | - | - | - | 73.54 ± 5.70 |